

# QUANTIFICATION OF WHITE MATTER USING DIFFUSION-TENSOR IMAGING

Hae-Jeong Park

Department of Diagnostic Radiology, Yonsei University, College of Medicine  
Seoul 120-749, Korea

- I. Introduction
- II. Diffusion in the Brain
  - A. Introduction to Diffusion in the Brain
  - B. Diffusion Coefficient
- III. Basics of DTI
  - A. Diffusion and Nuclear Magnetic Resonance Signals
  - B. DWI
  - C. DTI
- IV. Quantification of Diffusion Tensors
  - A. Scalars, Vectors, and Tensors
  - B. Quantification of Diffusion Tensors
  - C. Maps of the Quantitative Diffusion Index
  - D. Physiology of Anisotropic Diffusion
- V. DTI: Acquisition and Artifacts
  - A. *b*-Values and Gradient Vectors
  - B. Imaging Artifacts
  - C. Practical Considerations in the Acquisition of Diffusion-Tensor Images
- VI. Visualization of Diffusion Tensors
  - A. Color-Coded Vector Maps
  - B. Arrow-Vector Map
  - C. Three-Dimensional Tensor Maps
- VII. Basics of Fiber Tractography
  - A. Continuous Tensor Fields
  - B. Basic Streamline Propagation
  - C. Problems in Fiber Tractography
  - D. Regularized Streamline Algorithms
- VIII. Advances in Fiber Tractography
  - A. Connectivity Mapping
  - B. High-Angular-Resolution Diffusion Imaging
- IX. Quantification of White Matter using DTIs
  - A. ROI-Based Analysis of DTIs
  - B. Voxel-Based Statistical Parametric Mapping of DTIs
  - C. Fiber Tractography-Based Analysis of DTIs
  - D. Practical Considerations in the Analysis of DTIs
- X. Applications of DTI
- XI. Conclusion
- References

## I. Introduction

Diffusion-tensor magnetic resonance imaging (DT-MRI), also known simply as diffusion-tensor imaging (DTI), has rapidly evolved as a new *in vivo* approach to the investigation of white-matter abnormalities or tissue damages: quantifying the diffusivity of the water molecules in brain. The quantification of water diffusion *in vivo* is based on the characteristic movement of water molecules, which varies depending upon the tissue. For example, in pure liquids, such as cerebrospinal fluid, the motion of individual water molecules is random, meaning it has equal probability in all directions. However, the movement of water molecules within myelinated fibers is substantially restricted along the direction perpendicular to the orientation of the axons. Consequently, in white-matter fiber tracts, the principal direction of the water diffusion represents the direction of the fiber bundles. Thus, connecting points along the principal direction of the diffusion makes it possible to appreciate white-matter tracts within the brain. Such fiber-tracking schemes, often referred to collectively as fiber tractography, provide important information about the connectivity between brain regions. Therefore, DTI provides a quantitative assessment of the tissue-specific diffusivity and also provides information on anatomical connection. This chapter will focus on the basics and current advances of DTI for the quantification of white matter.

## II. Diffusion in the Brain

### A. INTRODUCTION TO DIFFUSION IN THE BRAIN

Diffusion is the random motion of an ensemble of particles. This is easily observed when a drop of ink is added to water, or when smoke dissipates into the air. The phenomenon of diffusion is named Brownian motion after the Scottish botanist Robert Brown, who in 1827 observed the random motion of minute pollen grains suspended in water. Diffusion is affected by the properties of the medium in which it occurs. Equal, or isotropic, diffusion occurs when a medium does not restrict molecular motion, as is the case with water. Skewed, or anisotropic, diffusion, as is seen within crystals and polymer films, is not equal in all directions.

This diffusion phenomenon has been successfully adopted as a very important marker for the tissue architecture in the brain. Diffusion in the brain, mainly of water molecules, has tissue-specific characteristics. In the cerebrospinal fluid, which has no specific directional restrictions, the diffusion is isotropic (i.e., there is equal probability of motion in all directions), as shown in [Fig. 1a](#). In white matter,

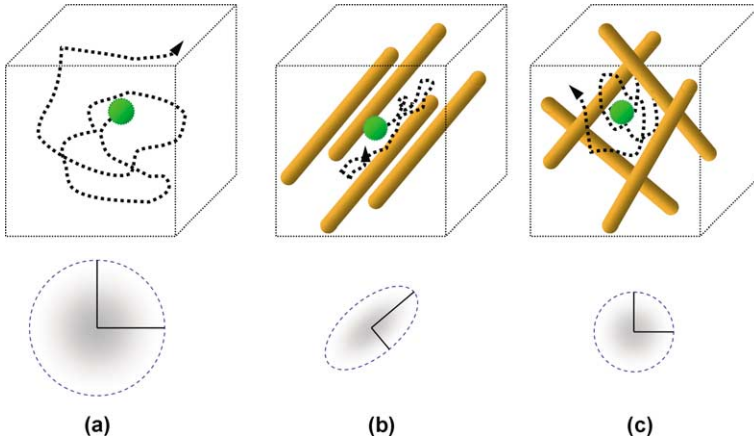


FIG. 1. Diffusion of the water molecule. Unrestricted isotropic self-diffusion (a), restricted anisotropic diffusion in well-arranged structures (b), and restricted isotropic diffusion in complex structures (c).

well-organized tissue structures such as neuronal fibers and myelin sheaths guide the water molecules along the direction of the fiber tracts, and the net diffusion process appears anisotropic (Fig. 1b). The mixture of tissue structures in gray matter—including axons, interconnecting dendrites along the layer, and cell bodies—restricts diffusion, thereby making the net diffusion isotropic (Fig. 1c).

## B. DIFFUSION COEFFICIENT

A typical approach to characterizing the diffusive transport of particles begins with Fick's first law of diffusion, which states that the diffusion flux  $\mathbf{j}$  is equal to the multiplication of a diffusion coefficient  $D$  and the negative gradient of concentration  $c$ :

$$\mathbf{j} = -D\nabla c \quad (1)$$

Measurement of this diffusion coefficient  $D$  makes it possible to characterize the diffusion process under particular structures.

Another approach to deriving the diffusion coefficient is to measure the root-mean-squared distance of the particles. Einstein showed that a diffusion coefficient  $D$  could be derived from the variance of the conditional probability distribution at a specific location for a specific duration. The root-mean-squared distance under unrestricted diffusion in  $d$ -dimensional space is described by

$$r_{rms} = \sqrt{2dDt} \quad (2)$$

i.e., Einstein's equation, where the diffusion coefficient  $D$  has dimensions of distance squared divided by time (e.g.,  $\text{mm}^2/\text{s}$ ).

If we can measure the change of magnetic resonance (MR) signal intensity according to the root-mean-squared distance of the water particles, we can derive the diffusion coefficient in the brain tissue. By introducing a diffusion-weighting magnetic gradient to a given sample, we can estimate the diffusion coefficient from the MR signal.

### III. Basics of DTI

#### A. DIFFUSION AND NUCLEAR MAGNETIC RESONANCE SIGNALS

This section assumes that the reader has a basic knowledge of MRI principles and so will cover only the rudimentary basics of NMR to explain the relationship between diffusion and nuclear magnetic resonance (NMR) signaling. Further details can be found in books that explain the principles of MRI. Under a magnetic field  $B_0$ , spinning protons undergo precession around the axis parallel to the magnetic field  $B_0$  with the rate of precession given by the Lamor equation:

$$f = \gamma B_0 \quad (3)$$

in which  $\gamma$  is the gyromagnetic ratio in MHz/Tesla for the spin under consideration. An external  $90^\circ$  radiofrequency (RF) pulse alternating with Lamor frequency excites the net magnetization of the spins to lie in the transverse plane perpendicular to  $B_0$  and renders all spins coherent in phase (the excitation process). After the RF signal is turned off, the transverse component of the net magnetization decays exponentially as individual protons dephase with a relaxation time constant,  $T_2$ , which varies depending on the tissue characteristics (the relaxation process). To generate the  $T_2$ -weighted image, we detect the difference in the magnitude of tissue-specific free-induction decay of the transverse magnetization. This  $T_2$ -weighted imaging, as are most other structural MRI techniques, is based on the assumption that the excitation and relaxation processes of a spin occur at stationary positions, changing only in the orientation of the spin. In contrast, the diffusion-weighted imaging (DWI) utilizes the spin translation under the gradient magnetic field. The gradient magnetic field has both strength and direction that can be represented by a vector  $\mathbf{G}$  (i.e.,  $d\mathbf{B}(\mathbf{x})/dx$ , where  $\mathbf{B}(\mathbf{x})$  is the magnetic field at the location  $\mathbf{x}$ ) (Fig. 2a). The phase accumulation of a spin for time duration  $\delta$  under a constant magnet field gradient  $\mathbf{G}$  can be written as a function of the spin location  $\mathbf{x}(t)$ , as

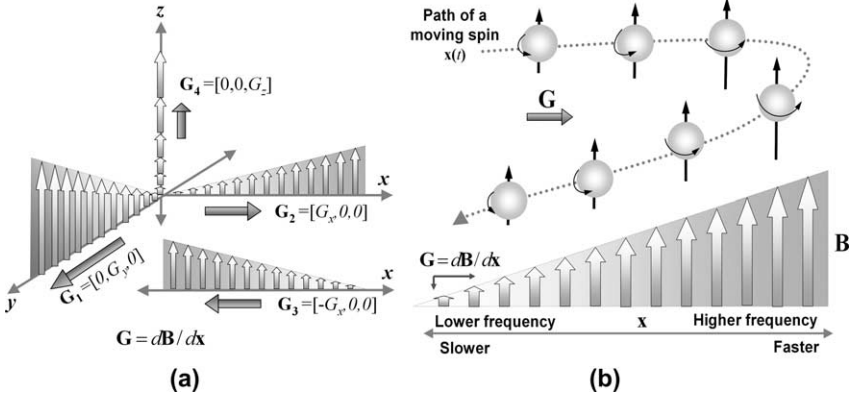


FIG. 2. Nonstationary spin in the magnetic-field gradient. The gradient of the magnetic field ( $\mathbf{B}$ ) can be represented with a vector ( $\mathbf{G}$ ) that has  $x$ ,  $y$ , and  $z$  components in three-dimensional space. Among the four examples of gradients in (a),  $\mathbf{G}_1$  is highest in strength, i.e., ( $G_y > G_x > G_z$ ), and it has the direction along the  $y$ -axis.  $\mathbf{G}_2$  and  $\mathbf{G}_3$  have only  $x$ -components, and  $\mathbf{G}_2$  is in the opposite direction to  $\mathbf{G}_3$ . Under the magnetic-field gradient, a spin rotates with a different precession frequency corresponding to the magnetic-field strength defined proportionally to the location of the spin (b). When a spin moves in the direction of the stronger magnetic field, the spin rotates faster, and vice versa.

$$\phi = \gamma \int_0^\delta \mathbf{G} \cdot \mathbf{x}(t) dt \quad (4)$$

in which a dot operation implies the location  $\mathbf{x}(t)$  projected onto the gradient direction  $\mathbf{G}$ . Note that  $\mathbf{G} \cdot \mathbf{x}(t)$  is the strength of the magnetic field at position  $\mathbf{x}(t)$  and is equal to the precession frequency of the spin when multiplied by  $\gamma$ , the gyromagnetic ratio, i.e.,  $f = \gamma B_0$ . When  $\mathbf{x}(t)$  is stationary for the time duration  $\delta$ , the phase accumulation is simply proportional to the multiplication of the magnitude of  $\mathbf{G}$  and position  $x_G$ , a projected position of  $\mathbf{x}$  along the direction of  $\mathbf{G}$ , i.e.,  $\phi = \gamma |\mathbf{G}| x_G \delta = \gamma |\mathbf{B}(x_G)| \delta = f \delta$ .

When a spin moves along the direction of the magnetic-field gradient, phase accumulation becomes more complex, depending on the path  $\mathbf{x}$  on which the spin moves. As illustrated in Fig. 2b, translation along the gradient magnetic-field direction will lead a spin through a varying magnetic field. The spin will have a higher or lower precession frequency when it moves along a higher or lower field. When multitudes of spinning protons move randomly along the magnetic-field gradient, the accumulated phases of spins for a given duration will shift incoherently. The phase incoherence due to the random motion (i.e., the diffusion) of spinning protons is detected as a decrease in the transverse magnetization signal.

## B. DWI

### 1. Basics of DWI

DWI was developed to render the MRI sensitive to diffusion. There are various methods of DWI, but we shall discuss two basic methods: gradient-echo DWI and spin-echo DWI. The gradient-echo DWI, illustrated in Fig. 3, utilizes two magnetic fields of identical strength and duration but of opposite directional

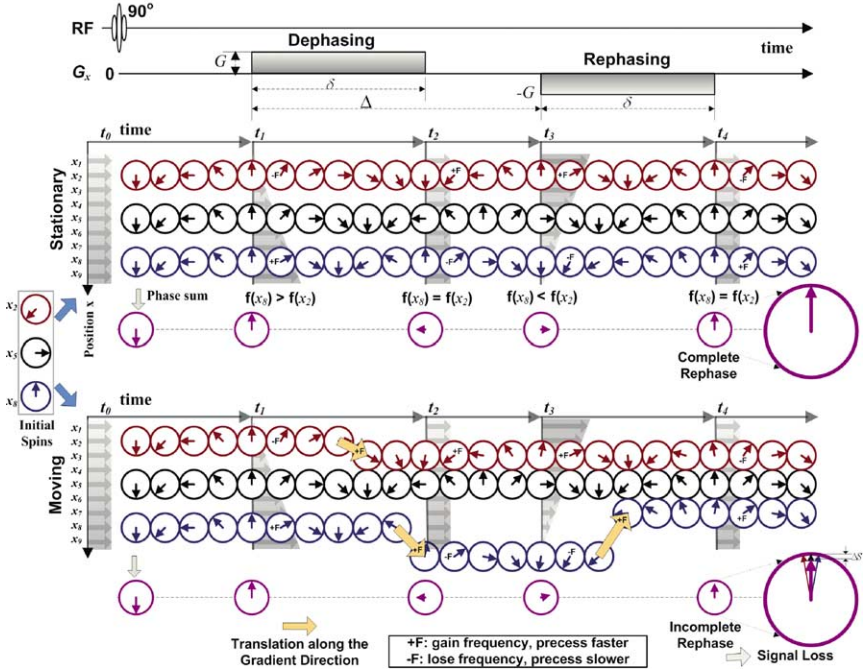


FIG. 3. Gradient-echo diffusion-weighted imaging (DWI). The phase accumulation of three spins initially located at  $x_2$ ,  $x_5$ , and  $x_8$  in the stationary situation (upper panel) and the moving situation (lower panel) during the gradient echo DWI sequence is explained as time elapses. A 90° excitation radiofrequency pulse renders all spins in phase ( $t_0$ ), and under the uniform magnetic field, this condition is sustained. When a first gradient magnetic pulse is applied ( $t_1$ ), the strength of the magnetic field increases along the  $x$ , i.e.,  $B(x_2) < B(x_5) < B(x_8)$ , and so does the precession frequency, i.e.,  $f(x_2) < f(x_5) < f(x_8)$ . The phase shifts accumulated due to the frequency difference will be sustained after the application of the uniform magnetic field, i.e.,  $G = 0$  ( $t_2$ ). The second magnetic-field gradient will cause the precession frequency at  $x_8$  to be lower than that at  $x_2$ . The passing of the same amount of accumulation time ( $\delta$ ) as for the first gradient magnetic pulse will lead to a complete phase realignment of all spins that are stationary (upper panel). For moving situations, the first spin (initially located at  $x_2$ ) moves to  $x_3$ , which causes the spin to rotate faster than at the previous position rotating with  $f(x_2)$ . Under the second gradient, the compensating phase accumulates proportionally to the frequency  $f(x_3)$ , which results in incomplete rephase of the phase accumulation with rotation frequency of both  $f(x_2)$  and  $f(x_3)$  during the first gradient (lower panel). The spin at  $x_8$  also undergoes similar incomplete rephase at time  $t_4$ .

gradients. For simplicity, we shall ignore the dephasing due to the spin and spin interaction, which causes free-induction decay of the T2 signal. After a 90° excitation RF pulse, all randomly phased stationary spins align and stay in phase under the homogeneous magnetic field. When the first gradient magnetic pulse is applied, the precession frequencies of protons depend on their location, as the strength of the magnetic field is proportional to the location of the spin. Spins in a weak magnetic field rotate slowly, whereas precession is faster in a strong magnetic field. During the time period of  $\Delta$ , the phase difference between spins accumulates. When the first gradient is turned off, all spins run with the same frequency, and thus the phase difference is sustained until they experience a new gradient pulse. When the second magnetic-field gradient pulse (with the same strength and duration but in the opposite gradient direction from the first one) is applied, it will cause the spins that were rotating faster at the previous gradient field to rotate more slowly, and vice versa. At the end of the second gradient, all stationary spins will have a coherent phase, which leads to a peak signal amplitude in the receiver coil. The upper panel of Fig. 3 shows the phase changes of the three stationary spins at different locations as time elapses. When spins under the gradient magnetic field move along the gradient direction (lower panel of Fig. 3), the spins will gain or lose the frequency according to their path. Therefore, the second gradient will not completely rephase the translating spins. We detect an attenuated signal of the net magnetization due to their incomplete rephase.

Instead of using two opposite gradient magnetic fields, the spin-echo pulse sequence (Stejskal and Tanner, 1965), as shown in Fig. 4, uses one strong identical diffusion-weighting gradient pulse on each side of the 180° refocusing pulse. The first pulsed gradient accumulates phase shifts for all spins, depending on their position and motion during the application of the first gradient. The 180° pulse inverts the phase of the spins, and the second gradient will induce another phase shift, thus canceling out the phase shifts for the stationary spins (the upper six spins in Fig. 4). Spins that have changed positions during the time period  $\Delta$  (the lower six spins in Fig. 4) will experience different phase shifts due to the two gradient pulses, and thus they will not become completely refocused. This incomplete phase realignment will consequently lead to signal attenuation.

Signal attenuation due to water diffusion, initially derived by Stejskal and Tanner (1965) based on spin-echo sequence, can be defined by the relationship between the diffusion-weighted signal,  $S$ , and the non-diffusion-weighted signal,  $S_0$ , as below:

$$S = S_0 \exp(-bD)$$

$$b \equiv \gamma^2 |\mathbf{G}|^2 \delta^2 (\Delta - \delta/3) \quad (5)$$

where the gradient factor,  $b$ , is determined by the diffusion-sensitizing gradient having strength  $|\mathbf{G}|$  for the duration  $\delta$ , with the time delay  $\Delta$  between the two diffusion-gradient pulses.  $\gamma$  is the gyromagnetic ratio of proton of the water

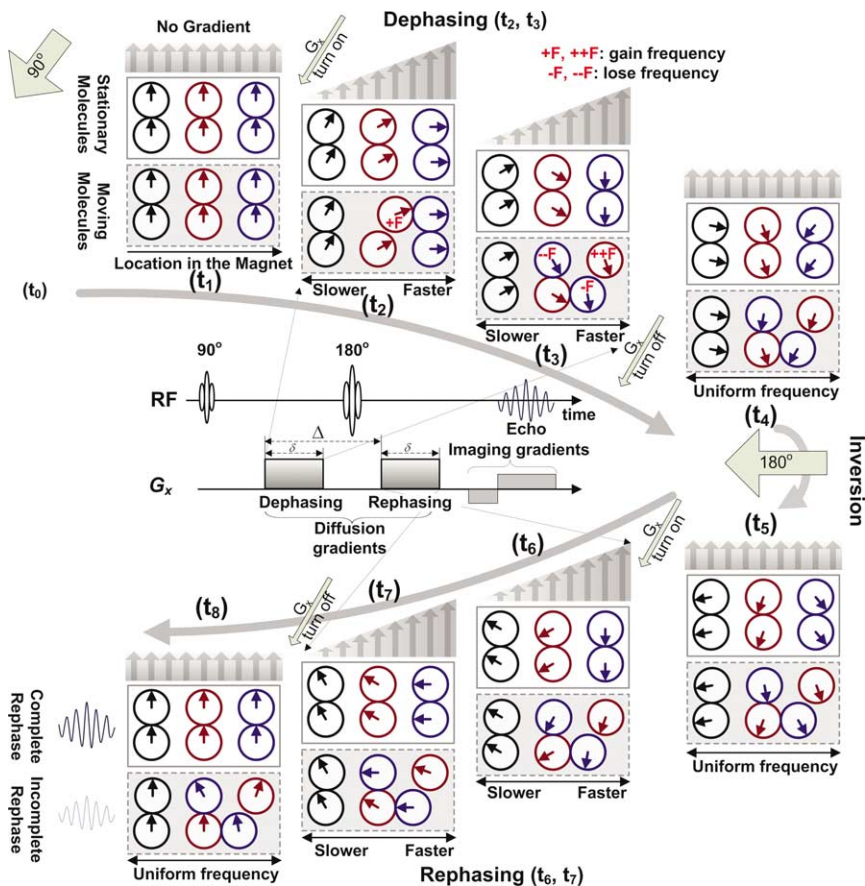


FIG. 4. Spin-echo diffusion-weighted imaging. The time courses of the phase accumulations of six stationary molecules (upper part) and of six moving molecules (lower part) are explained for the spin-echo sequence. Under the uniform magnetic field with no gradient ( $t_1$ ), the phase alignment of all individual spins caused by a  $90^\circ$  radiofrequency excitation is sustained. When the first gradient magnetic pulse is on ( $t_2$  and  $t_3$ ), the location-dependent magnetic fields induce spins to rotate with different frequencies. If a spin moves along the direction of the magnetic-field gradient, the phase of the spin changes. A  $180^\circ$  radiofrequency pulse reverses the phase of all spins ( $t_4$  and  $t_5$ ). The second gradient ( $t_6$  and  $t_7$ ) will lead to realignment for a stationary spin ( $t_8$ ), whereas moving molecules will be rendered out of phase. This out-of-phase condition leads to signal attenuation.

molecule (42 MHz/Tesla). The non-diffusion-weighted signal,  $S_0$ , is a T2-weighted signal at the echo time (TE), i.e., the time from RF excitation pulse to the center of the echo being received. The diffusion coefficient  $D$  reflects molecular “diffusivity” along the direction of the magnetic-field gradient  $\mathbf{G}$ . Since the diffusion coefficient  $D$  measured at a voxel can also be affected by many things—tissue perfusion, the



partial volume averaging effects, and other experimental errors—it is often called the “apparent” diffusion coefficient (ADC). By measuring the voxel-level signal attenuation under a single magnetic-field gradient, we can derive the ADC  $D$  at all voxels in the entire brain composing a diffusivity map (Le Bihan *et al.*, 1986).

With the previously determined  $b$  value for NMR acquisition and the measured diffusion weighted signal  $S$ , Eq. 5 can be reduced to the relationship between two unknown variables, the ADCs  $D$  and  $S_0$ . In order to take out  $S_0$  and derive the ADC  $D$ , it is necessary to acquire the diffusion-weighted images with at least two different  $b$ -values. The ADC  $D$  can be derived from two DWIs as follows:

$$\begin{aligned} S(b_0) &= S_0 \exp(-b_0 D) \\ S(b_1) &= S_0 \exp(-b_1 D) \\ D &= -\frac{1}{b_1 - b_0} \ln \left( \frac{S(b_1)}{S(b_0)} \right) \end{aligned} \quad (6)$$

The ADC  $D$  is the slope representing the logarithmic difference of attenuation according to the different  $b$ -values, as in Fig. 5.

In practice, instead of acquiring two different  $b$ -values, researchers often choose  $b_0$  to be zero, which yields  $S(b_0) = S_0$ , a T2-weighted image without diffusion weighting. Therefore, we can derive the ADC  $D$  by acquiring a DWI at a single  $b$ -value and a non-diffusion-weighted T2 reference image. One must remember that the signal attenuation due to phase incoherence is caused by both

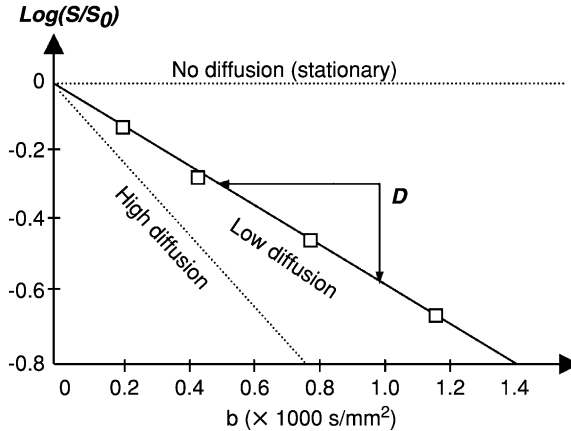


FIG. 5. Diffusion coefficient and diffusion factor  $b$ -values. We can derive diffusion coefficient  $D$  by calculating the slope of  $\log(S/S_0)$  at two or more  $b$ -values. Most diffusion-imaging sequences use a  $b$ -value on the order of  $1000 \text{ s/mm}^2$ .

the diffusion process ( $\propto \exp(-bD)$ ) and the T2 relaxation process ( $\propto \exp(-TE/T2)$ ), but the relaxation effects are nicely cancelled out by the division term of Eq. 6 in the spin-echo sequence.

### C. DTI

#### 1. Tensor Representation of Three-Dimensional Diffusion

We have discussed DWI that measures the attenuation of the NMR signal when multitudes of spins randomly move along the direction of a given magnetic-field gradient. In other words, a single magnetic-field gradient can describe the motion along a single direction. In fact, the random motion of water molecules in the brain tissue occurs in three-dimensional space, and the mobility may not be the same in all directions. In order to quantify diffusion, traditional DWI has measured NMR attenuation due to diffusion along the three laboratory coordinates (x-axis, y-axis, and z-axis) and has derived three diffusion coefficients, or diffusivities,  $D_{xx}$ ,  $D_{yy}$ , and  $D_{zz}$ .  $D_{xx}$ ,  $D_{yy}$ , and  $D_{zz}$  indicate the diffusivities along the x-axis, y-axis, and z-axis of the laboratory coordinate system, respectively. Using these diffusivities measured along the three orthogonal axes, an isotropic diffusion, as in Fig. 6a, and an anisotropic diffusion aligned precisely along the laboratory coordinates, as in Fig. 6b, can be described. However, three diffusion coefficients cannot fully describe the three-dimensional anisotropic diffusion, which is not aligned with the laboratory coordinates, as shown in Fig. 6c.

Therefore, it is an essential requirement that diffusivities be measured at additional directions for the complete description of any diffusion process. By including the diffusion components along the x and y direction, the x and z

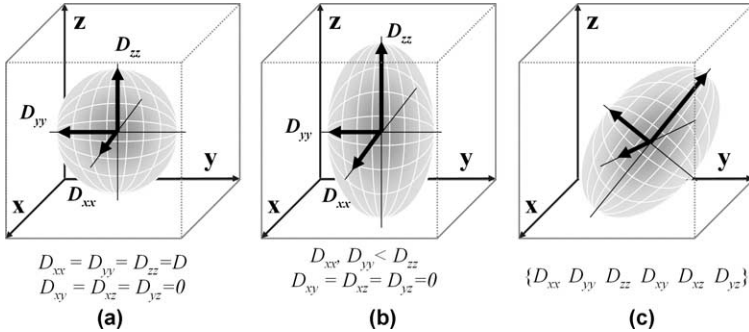


FIG. 6. Representation of isotropic and anisotropic diffusion. Isotropic diffusion, which has the same diffusivity in all directions, and anisotropic diffusion, in which the principal directions of diffusivity align with three MRI coordinates, can be described using only three diffusion coefficients,  $D_{xx}$ ,  $D_{yy}$ , and  $D_{zz}$ . However, six diffusion coefficients are necessary to fully describe the three-dimensional diffusion.

direction, and the y and z direction (i.e.,  $D_{xy}$ ,  $D_{xz}$ , and  $D_{yz}$ ) in addition to the traditional measurements of diffusivities along the x-, y-, and z-axes (i.e.,  $D_{xx}$ ,  $D_{yy}$ ,  $D_{zz}$ ), it is possible to document the three-dimensional diffusion process. These six diffusivities can be mathematically represented as a symmetric matrix, called the “tensor” as shown in Eq. 7:

$$\mathbf{D} = \begin{pmatrix} D_{xx} & D_{xy} & D_{xz} \\ D_{xy} & D_{yy} & D_{yz} \\ D_{xz} & D_{yz} & D_{zz} \end{pmatrix} \quad (7)$$

The tensor comprises the multiple-directional geometry of diffusion in a three-dimensional space. This diffusion-tensor matrix can be related to a covariance matrix of the three-dimensional Gaussian displacement distribution that explains the probability distribution of the displacement of a single spin for a unit time. The basic properties of the tensor will be discussed in detail in Section IV.

## 2. Derivation of Diffusion Tensors

Diffusion-tensor imaging was originally developed by Bassler *et al.* (1994) for three-dimensional assessment of diffusion data *in vivo*, achieved by measurement of DWIs along more than six directional gradients. In order to document the diffusion phenomena, three-dimensional DTI utilizes the diffusion tensor instead of a single diffusion coefficient in the DWI in Eq. 5. Signal attenuation due to the diffusion under the magnetic-field gradient  $\mathbf{G} = [G_x \ G_y \ G_z]$  becomes:

$$S = S_0 \exp(-\mathbf{b} \cdot \mathbf{D}) = S_0 \exp\left(-\sum_{i=1}^3 \sum_{j=1}^3 b_{ij} D_{ij}\right), \quad i, j = x, y, z \quad (8)$$

where  $b_{ij} = -\gamma^2 \delta^2 (\Delta - \delta/3) G_i G_j$ ,  $i, j = x, y, z$  for the spin-echo sequences is an element of the gradient factor matrix  $\mathbf{b}$ . Equation 8 is the more generalized form of Eq. 5, which can be applicable to either anisotropic or isotropic diffusion. An isotropic diffusion can be derived simply by replacing the tensor matrix  $\mathbf{D}$  with  $D\mathbf{I}$ , i.e., the identity matrix multiplied by diffusivity  $D$ . Equation 8 can be rewritten as

$$\begin{aligned} \ln \left[ \frac{S}{S_0} \right] &= -\mathbf{b} \cdot \mathbf{D} \\ &= -[b_{xx} D_{xx} + b_{yy} D_{yy} + b_{zz} D_{zz} + 2b_{xy} D_{xy} + 2b_{xz} D_{xz} + 2b_{yz} D_{yz}] \\ &= -\overline{\mathbf{b}} \cdot \overline{\mathbf{D}} \end{aligned} \quad (9)$$

where

$$\begin{aligned} \overline{\mathbf{b}} &= [b_{xx} \ b_{yy} \ b_{zz} \ 2b_{xy} \ 2b_{xz} \ 2b_{yz}] \\ \overline{\mathbf{D}} &= [D_{xx} \ D_{yy} \ D_{zz} \ D_{xy} \ D_{xz} \ D_{yz}] \end{aligned}$$

For the derivation of the diffusion tensor matrix  $\mathbf{D}$  with six independent variables from Eq. 9, at least six equations are required. Therefore, six diffusion measurements along the noncollinear noncoplanar gradient directions, plus one non-diffusion-weighted measurement as the reference datum, are required in order to obtain the complete solution.

Figure 7 shows examples of these seven images, where  $S_0$  is the non-diffusion-weighted image and  $S_1, S_2, S_3, S_4, S_5$ , and  $S_6$  are the DWIs derived from the six different diffusion-sensitizing magnetic gradients,  $\mathbf{G}$ . From these data sets, a complete set of equations are illustrated below:

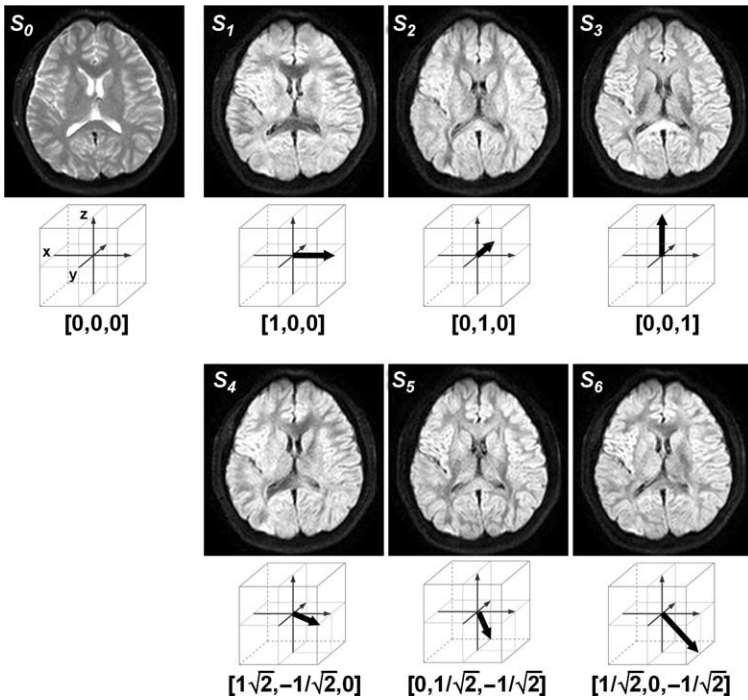


FIG. 7. Diffusion-weighted images measured along six magnetic gradients ( $S_1, \dots, S_6$ ) and non-diffusion-weighted image ( $S_0$ ). The black arrow indicates the direction of the magnetic-field gradient used to derive each diffusion-weighted image. For high diffusion, the random phase shifts suppress the transverse magnetization signal; these are represented with dark pixels in the diffusion-weighted image. In contrast, the low diffusion leads to a small suppression of signal, causing the diffusion-weighted image's pixels to appear brighter. In the  $S_1$  image measured along the left-right direction, the regions that diffuse highly along this direction, such as the corpus callosum, have high signal attenuation and thus low intensity. The internal capsule, which appears dark at the  $S_3$  image, is measured along the inferior-superior direction. By combining these seven images, we can derive a diffusion-tensor image.

$$\begin{aligned} \ln \left[ \frac{S_1}{S_0} \right] &= -\bar{\mathbf{b}}_1 \cdot \bar{\mathbf{D}}, \ln \left[ \frac{S_2}{S_0} \right] = -\bar{\mathbf{b}}_2 \cdot \bar{\mathbf{D}}, \ln \left[ \frac{S_3}{S_0} \right] = -\bar{\mathbf{b}}_3 \cdot \bar{\mathbf{D}}, \\ \ln \left[ \frac{S_4}{S_0} \right] &= -\bar{\mathbf{b}}_4 \cdot \bar{\mathbf{D}}, \ln \left[ \frac{S_5}{S_0} \right] = -\bar{\mathbf{b}}_5 \cdot \bar{\mathbf{D}}, \ln \left[ \frac{S_6}{S_0} \right] = -\bar{\mathbf{b}}_6 \cdot \bar{\mathbf{D}} \end{aligned} \quad (10)$$

Since  $S_0, S_1, \dots$ , and  $S_6$  are measured, and  $\bar{\mathbf{b}}_1, \bar{\mathbf{b}}_2, \dots, \bar{\mathbf{b}}_6$  are previously assigned, the diffusion coefficients  $D_{xx}, D_{yy}, D_{xz}, D_{yz}$ , and  $D_{zz}$  can be derived from the solutions of the linear equations (Eq. 10). Note that the diffusion tensors are calculated voxel by voxel in the entire brain. The resultant diffusion-tensor components of the DWIs in Fig. 7 are displayed in Fig. 8.

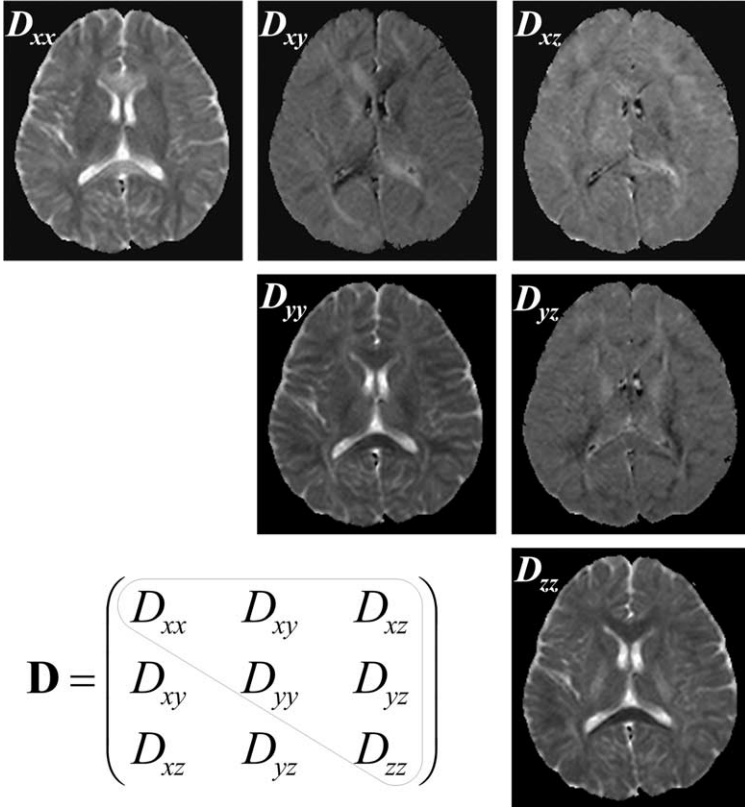


FIG. 8. Diffusion-tensor image. The six components of a diffusion-tensor image derived from the six diffusion-weighted images and a non-diffusion-weighted image (from Fig. 7) is displayed. High signal attenuation along the left-right direction in the corpus callosum is presented with low intensity in  $S_1$  in Fig. 7 but with high intensity in the diffusion-tensor image,  $D_{xx}$ .

#### IV. Quantification of Diffusion Tensors

##### A. SCALARS, VECTORS, AND TENSORS

In physical applications, certain quantities (such as temperature and mass) possess only magnitude. A quantity that can be represented by a single real number is called a “scalar.” Quantities such as force and velocity, which possess both magnitude and direction, can be represented by arrows that have length and direction from a given reference point, and these are called “vectors.” More complex geometric or physical quantities, such as strain and diffusion, are multidirectional entities that can be represented by what are known as “tensors.”

A tensor, which contains multidirectional information, can be resolved into three orthogonal vectors and their magnitudes by the mathematical operation known as diagonalization. Orthogonal unit vectors, also called eigenvectors, represent the principal directions of a tensor. The magnitudes are represented by scalars, or eigenvalues.

$$\begin{aligned}
 \mathbf{D} &= \begin{pmatrix} D_{xx} & D_{xy} & D_{xz} \\ D_{xy} & D_{yy} & D_{yz} \\ D_{xz} & D_{yz} & D_{zz} \end{pmatrix} \\
 &= [\mathbf{e}_1 \quad \mathbf{e}_2 \quad \mathbf{e}_3]^T \begin{pmatrix} \lambda_1 & 0 & 0 \\ 0 & \lambda_2 & 0 \\ 0 & 0 & \lambda_3 \end{pmatrix} [\mathbf{e}_1 \quad \mathbf{e}_2 \quad \mathbf{e}_3] \\
 &= \lambda_1 \mathbf{e}_1 \mathbf{e}_1^T + \lambda_2 \mathbf{e}_2 \mathbf{e}_2^T + \lambda_3 \mathbf{e}_3 \mathbf{e}_3^T = \sum_{k=1}^3 \lambda_k \mathbf{e}_k \mathbf{e}_k^T \quad (11)
 \end{aligned}$$

where  $\mathbf{e}_1$ ,  $\mathbf{e}_2$ , and  $\mathbf{e}_3$  are eigenvectors and  $\lambda_1$ ,  $\lambda_2$ , and  $\lambda_3$  are eigenvalues obtained by diagonalization of the tensor matrix. For diffusion tensors,  $\lambda_1$ ,  $\lambda_2$ , and  $\lambda_3$  indicate diffusivity along the directions  $\mathbf{e}_1$ ,  $\mathbf{e}_2$ , and  $\mathbf{e}_3$ , respectively. The eigenvalues are often denoted in a sorted order ( $\lambda_1 \geq \lambda_2 \geq \lambda_3$ ), and the eigenvector  $\mathbf{e}_1$  that is associated with the maximal eigenvalue  $\lambda_1 > \lambda_2, \lambda_3$ , (which will be called the major eigenvector throughout this paper) implies the principal direction of the diffusion.

As shown in Fig. 9, a diffusion tensor derived from more than directional measurements can be conceived in terms of the ellipsoidal model, where each eigenvector corresponds to the principal axis of the ellipsoid and the eigenvalues indicate the extent of the ellipsoid along the corresponding axis.

##### B. QUANTIFICATION OF DIFFUSION TENSORS

Because the diffusion process of the tissue underlying a voxel can be modeled as an ellipsoid, the scalar indices for the size and shape (i.e., eccentricity) of the ellipsoidal diffusion can be represented by the combination of eigenvalues that

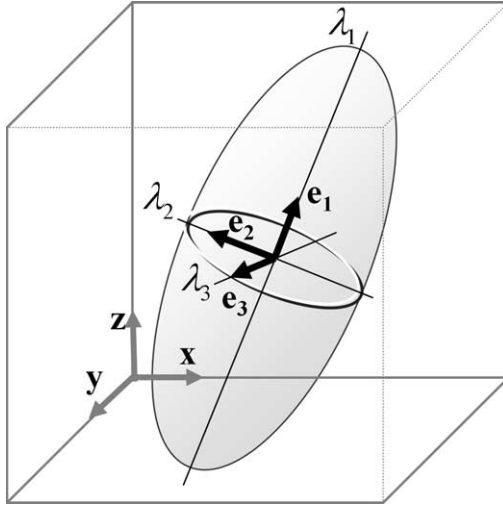


FIG. 9. Eigenvectors and eigenvalues of a diffusion tensor: Diffusion tensors can be better described by a new coordinate system of eigenvectors,  $\mathbf{e}_1$ ,  $\mathbf{e}_2$ , and  $\mathbf{e}_3$ , and their eigenvalues  $\lambda_1$ ,  $\lambda_2$ , and  $\lambda_3$ , derived by diagonalization of the diffusion tensor.  $\mathbf{e}_1$ ,  $\mathbf{e}_2$ , and  $\mathbf{e}_3$  are the principal axes of the ellipsoidal model of the diffusion. The eigenvalues are denoted in a sorted order  $(\lambda_1, \lambda_2, \lambda_3)$ , and an eigenvector corresponding to any of the largest eigenvalues ( $\lambda_1$ ) is often denoted  $\mathbf{e}_1$  and called a major eigenvector. The diffusion distance along an eigenvector for a unit of time is proportional to the square root of the corresponding eigen value, i.e.,  $\sqrt{i}$

are insensitive to the orientation of the diffusion, the direction of the gradient magnetic fields, and the laboratory coordinates. The most prevalent scalar indices used to quantify the diffusion tensor are the mean ADC and anisotropy.

### 1. The Mean ADC

The mean ADC, also called mean diffusivity, can be defined by a third of the trace, which is the sum of diagonal elements of the matrix, which also equals the sum of all the eigenvalues.

$$\begin{aligned} \langle ADC \rangle &= \text{Trace}(\mathbf{D})/3 = (D_{xx} + D_{yy} + D_{zz})/3 \\ &= (\lambda_1 + \lambda_2 + \lambda_3)/3 = \langle \lambda \rangle \end{aligned} \quad (12)$$

In isotropic diffusion, the mean ADC can be measured by an ADC measured along one of the  $x$ , the  $y$ , or the  $z$  direction. The mean ADC of anisotropic diffusion represents the ADC of the equivalent isotropic diffusion.

### 2. The Anisotropy Index

An anisotropic index is defined to characterize the eccentricity of the ellipsoidal diffusion in a scale-independent and coordinate-independent way. Relative anisotropy (RA) and fractional anisotropy (FA) (Basser and Pierpaoli, 1996) are the most representative examples of anisotropic indices.

$$\begin{aligned}
RA &= \frac{\sqrt{(\lambda_1 - \langle \lambda \rangle)^2 + (\lambda_2 - \langle \lambda \rangle)^2 + (\lambda_3 - \langle \lambda \rangle)^2}}{\sqrt{3\langle \lambda \rangle}} \\
FA &= \frac{\sqrt{(\lambda_1 - \lambda_2)^2 + (\lambda_2 - \lambda_3)^2 + (\lambda_1 - \lambda_3)^2}}{\sqrt{2}\sqrt{(\lambda_1^2 + \lambda_2^2 + \lambda_3^2)}} \\
&= \frac{\sqrt{3[(\lambda_1 - \langle \lambda \rangle)^2 + (\lambda_2 - \langle \lambda \rangle)^2 + (\lambda_3 - \langle \lambda \rangle)^2]}}{\sqrt{2(\lambda_1^2 + \lambda_2^2 + \lambda_3^2)}} \tag{13}
\end{aligned}$$

where  $\langle \lambda \rangle = (\lambda_1 + \lambda_2 + \lambda_3)/3$ .

The RA is the normalized standard deviation that represents the ratio between an isotropic and an anisotropic component. The FA is the fraction of the magnitude of diffusion due to anisotropic diffusion. Both RA and FA are 0 for isotropic diffusion ( $\lambda_1 = \lambda_2 = \lambda_3$ ) and are 1 for ideal anisotropic diffusion (i.e.,  $\lambda_2 = \lambda_3 = 0$ ). RA changes linearly according to the changes of anisotropy, which is a good characteristic for the quantification of diffusion. However, RA is vulnerable to noise. FA is used prevalently, in spite of its nonlinearity, because of its robustness relative to noise.

Figure 10 shows examples of diffusion tensors with mean ADC and FA at the corpus callosum, prefrontal white matter, posterior limb of the internal capsule (PLIC), optic radiation, and cerebrospinal fluid. The FA at the posterior limb is close to 1, and the mean ADC is lower than that of any other tensor. The cerebrospinal fluid shows the highest mean ADC, with FA close to 0.

### 3. The Geometric Index

Diffusion can be decomposed into three geometric components: line, plane, and sphere (Westin *et al.*, 2002):

$$\mathbf{D} = c_l \mathbf{D}_l + c_p \mathbf{D}_p + c_s \mathbf{D}_s$$

where

$$\begin{aligned}
\mathbf{D}_l &= \lambda_1 \mathbf{e}_1 \mathbf{e}_1^T, \mathbf{D}_p = \lambda_1 (\mathbf{e}_1 \mathbf{e}_1^T + \mathbf{e}_2 \mathbf{e}_2^T), \\
\mathbf{D}_s &= \lambda_1 (\mathbf{e}_1 \mathbf{e}_1^T + \mathbf{e}_2 \mathbf{e}_2^T + \mathbf{e}_3 \mathbf{e}_3^T) \\
c_l &= \frac{\lambda_1 - \lambda_2}{\lambda_1}, c_p = \frac{\lambda_2 - \lambda_3}{\lambda_1}, c_s = \frac{\lambda_3}{\lambda_1} \tag{14}
\end{aligned}$$

$\mathbf{D}_l$ ,  $\mathbf{D}_p$ , and  $\mathbf{D}_s$  represent the geometric tensor matrix, composed solely of a line, a plane, and a sphere, respectively, and  $c_l$ ,  $c_p$ , and  $c_s$  are fractions of these geometric tensor matrices, the sum of which is equal to 1.



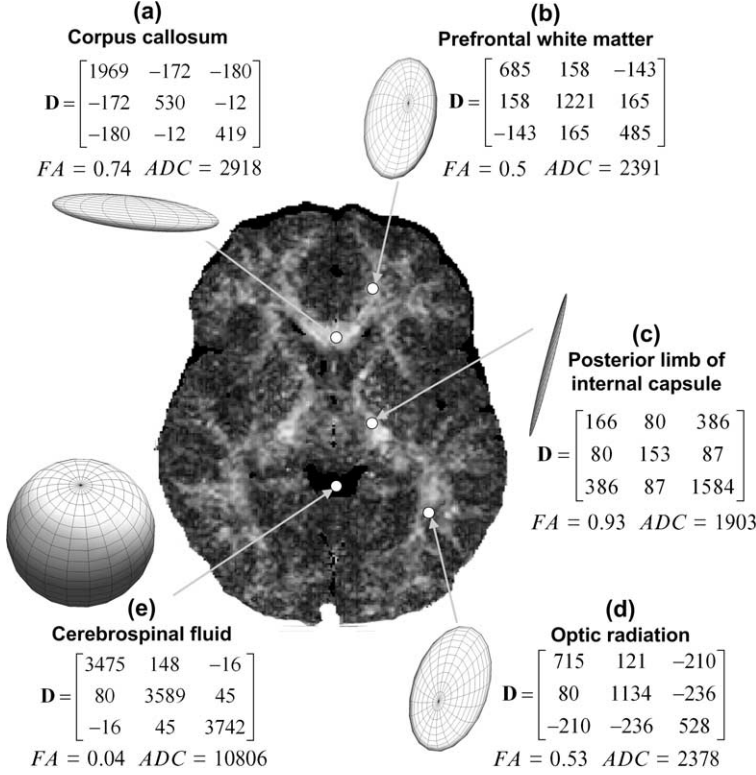


FIG. 10. Diffusion tensors in the brain. Diffusion tensors at (1) the corpus callosum, (2) the prefrontal white matter, (3) the posterior limb of the internal capsule, (4) the optic radiation, and (5) the cerebrospinal fluid are displayed with a fractional anisotropy image as a background image.

$$c_l + c_p + c_s = 1 \quad (15)$$

These geometric indices provide more detailed information about the shape of the diffusion at a specific region. Where diffusion occurs mostly in the direction associated with the largest eigenvector, i.e.,  $\lambda_1 \gg \lambda_2, \lambda_3$ ,  $c_l$  is 1 and the diffusion tensor  $\mathbf{D}$  consists mostly of the  $\mathbf{D}_l$  component, i.e.,  $\mathbf{D} \approx \mathbf{D}_l$ . Diffusion is restricted to a plane spanned by two eigenvectors associated with the first and second largest eigenvalues ( $\lambda_1 \approx \lambda_2 \gg \lambda_3$ ), in which case  $c_p$  is 1 and diffusion  $\mathbf{D}$  can be reduced to  $\mathbf{D}_p$ . In the case of complete isotropic diffusion ( $\lambda_1 = \lambda_2 = \lambda_3$ ),  $\mathbf{D}$  is equal to  $\mathbf{D}_s$ .

#### 4. The Lattice Anisotropy Index

In comparison with previous indices, which describe a diffusion quantity defined at a voxel, the scalar index for the pattern or distribution of diffusion

within a local neighborhood is defined in terms of macrostructural diffusion coherency, which is known as the “lattice index” (LI). An example of the lattice index for a tensor  $D$  at a voxel  $v$  is defined as in Eq. 16 (Pierpaoli and Basser, 1996; Westin *et al.*, 2002):

$$LI(v) = \sum_{k \in \mathbf{N}_v} a_k \left( \sqrt{\frac{3}{8}} \frac{\sqrt{\langle \mathbf{T}, \mathbf{T}_k \rangle}}{\sqrt{\langle \mathbf{D}, \mathbf{D}_k \rangle}} + \frac{3}{4} \frac{\langle \mathbf{T}, \mathbf{T}_k \rangle}{\sqrt{\langle \mathbf{D}, \mathbf{D} \rangle} \sqrt{\langle \mathbf{D}, \mathbf{D}_k \rangle}} \right) \quad (16)$$

where  $k$  is an element of set  $\mathbf{N}_v$  neighboring voxel  $v$ ,  $a_k$  is a weighted spatial mask,  $\langle \rangle$  is the tensor dot product, and  $\mathbf{T}$  is the anisotropic component of diffusion tensor  $\mathbf{D}$ , which can be written as

$$\mathbf{T} = \mathbf{D} - \frac{D_{xx} + D_{yy} + D_{zz}}{3} \mathbf{I} \quad (17)$$

The LI of a voxel is an intervoxel scalar quantity that depends on the directional coherence of the diffusion in the reference voxel with that in the neighboring voxels. The LI is very robust to random noise at a low signal-to-noise ratio (SNR). However, this robustness depends on acquisition parameters such as voxel size.

### C. MAPS OF THE QUANTITATIVE DIFFUSION INDEX

Scalar indices of each voxel listed above are used to contrast tissue types in the entire brain according to the characteristic of the index. Figure 11 shows exemplary contrast images according to the information that can be obtained from a diffusion-tensor image. A plain T2-weighted image provides anatomical references for gray matter, white matter, and cerebrospinal fluid spaces, as does a T1-weighted image. From three eigenvalues (i.e.,  $\lambda_1, \lambda_2$  and,  $\lambda_3$ ), mean ADC, FA,  $c_b$ ,  $c_p$ , and  $c_s$  images can be derived. Mean ADC implies the amount of diffusion, whereas FA provides the shape of diffusion, which is related to information about density and/or organization of the fiber tracts. An FA image conspicuously enhances white matter. A  $c_l$  component image shows similarity to an FA image. An LI image provides information regarding the coherence of the macroscopic fiber structures.

### D. PHYSIOLOGY OF ANISOTROPIC DIFFUSION

#### 1. Sources of Anisotropy in the Brain

The source of anisotropy in brain tissue is one of the most important issues in diffusion-tensor research, and it is not yet clearly understood. Among the several possibilities, the myelin sheath-encasing axon is the preferred hypothetical

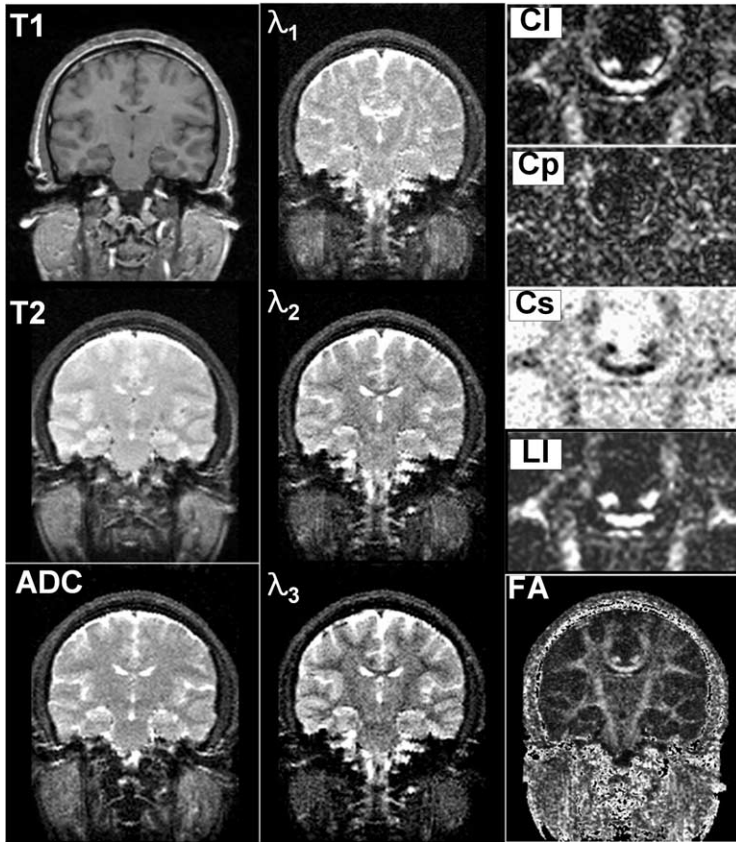


FIG. 11. Scalar indices of diffusion tensors. Coronal slices of several contrast images are displayed using scalar indices of the diffusion tensors. The T1 image is displayed for reference purposes. From three eigenvalues (i.e.,  $\lambda_1$ ,  $\lambda_2$ , and  $\lambda_3$ ), images of the mean apparent diffusion coefficient (ADC), fractional anisotropy (FA), and line, place, sphere component ( $c_b$ ,  $c_p$ , and  $c_s$ ) images are derived. LI: lattice index.

explanation of diffusion anisotropy; myelin is composed of numerous lipid bilayers, which limit the permeability of water and hinder water diffusion perpendicular to the fibers. However, fibers without myelin sheaths, such as nonmyelinated garfish olfactory nerves (Beaulieu and Allen, 1994) and neonate brains in which myelin has not yet appeared (Huppi *et al.*, 1998; Wimberger *et al.*, 1995), also exhibit diffusion anisotropy. Therefore, we know that myelin is not an essential component for anisotropic diffusion. Cylindrical neurofibrils and fast axonal transportation linked to the microtubules have not been found to be dominantly related to diffusion anisotropy (see Beaulieu [2002] for a detailed

review). As of this writing, it is believed that axonal membranes play a primary role, and that myelination, although it is not necessary for significant anisotropy, can modulate the degree of anisotropy.

## 2. *Macroscopic Anisotropy*

Although there are several factors that influence self-diffusion—for example, molecular weight, intermolecular interaction (viscosity), and temperature—the overall mobility of diffusion molecules in the brain depends mostly on their underlying microstructures. The degree of anisotropy is related to factors such as the density and diameter of axons, the degree of axon myelination, and the coherence of axon direction. It should be noted that structures that exhibit anisotropic diffusion at the molecular level can be isotropic at the macroscopic level when multiple fiber bundles cross or merge at a voxel. Therefore, it is not easy to directly relate a single factor to macroscopic anisotropy. Special care must be taken in the interpretation of any images obtained.

## V. DTI: Acquisition and Artifacts

### A. *b*-VALUES AND GRADIENT VECTORS

The *b*-value, seen in Eq. 5, is used in the order of  $1000 \text{ s/mm}^2$  in most diffusion imaging sequences. This value can be obtained by increasing the amplitude ( $|\mathbf{G}|$ ) and/or the duration ( $\delta$ ) of the diffusion-weighting gradients' lobes. The increased duration ( $\delta$ ) of the gradient, however, suffers from a long echo time, which results in longer acquisition time and unwanted contrast change due to the T2-weighted signal. In order to minimize the echo time, maximal amplitude of the magnet gradient ( $|\mathbf{G}|$ ) with faster slew rate is used to achieve the desired *b*-values. However, the rapid change of high-amplitude gradients may induce undesirable stimulation of the peripheral nerve and may induce geometry-distorting eddy currents, which will be discussed in the following section.

Although six orientation DWIs can be used to construct a diffusion-tensor image, in general, DWIs with a higher quantity of gradient orientations are employed to reduce the orientation bias in the parameters derived from the diffusion-tensor image. Thus, proper application of the number of gradient orientations and their distributions in three-dimensional space are both crucial for the precise measurement of anisotropic diffusion within the acceptable imaging time. Jones (2004) showed that more than 30 diffusion-weighted gradients evenly distributed in three-dimensional space are required to make robust tensor estimates. These optimal gradients, obtained by the concepts of the electrostatic repulsion algorithm, lead to a higher SNR and an improved contrast in the diffusion parameter of interest (e.g., FA or mean ADC).

## B. IMAGING ARTIFACTS

Many of the DTI techniques were developed in the process of reducing artifacts that often disturb the interpretation of data. Therefore, it is worthwhile to understand the artifacts in DTI.

### 1. *Motion Artifacts*

Since diffusion is a microscopic molecular movement, the outer macroscopic movement can disturb the detection of micro-scale diffusion. Macroscopic motion includes large-scale bulk motions and brain motions caused by pulsations in cerebrospinal fluid. These motions can cause artifacts such as ghosting, blurring, and misalignment of DWIs. Bulk motion is often removed by the application of rigid-body transformations in postprocessing. However, brain motion from pulsation of cerebrospinal fluid caused by the heartbeat is too complex to be removed with a rigid-body transformation. Although the pulsation effect is negligible for normal anatomical images, an extremely motion-sensitized DWI is substantially affected, especially in the period of 100–300 ms after systole (Norris, 2001). This pulsation of the brain can be partly reduced by the acquirement of images with cardiac triggering, but the cost is a longer acquisition time.

The most common approach to overcoming motion artifacts is to utilize a fast acquisition sequence, for example, a single-shot echo planar image EPI, which acquires a whole brain image in a single shot of about 100 ms. However, fast imaging sequences suffer from disadvantages such as low spatial resolution, geometric distortion (due to eddy currents and increased sensitivity to the susceptibility changes), low SNR, and image blurring. Multishot EPI is affected by less distortion than is single-shot EPI. However, it suffers from severe image artifacts due to subject motion, as a result of ultra-shot motion effects that are inconsistent between shots. To overcome this artifact, motion correction using navigator echoes is sometimes used for multishot DWI. Parallel imaging shows its usefulness in reducing acquisition time, reducing magnetic susceptibility artifacts, and increasing spatial resolution.

Another way to reduce motion artifacts is to use motion-insensitive sequences such as line scan diffusion-weighted imaging(LSDI) (Maier *et al.*, 1998). Acquirement of a two-dimensional image line by line using LSDI does not require phase-encoding steps and is insensitive to bulk motion and susceptibility artifacts but is limited by its time efficiency.

### 2. *Eddy Currents*

Eddy currents are small electrical currents that are found in electrically conductive structures of the MRI scanner. These eddy currents are induced by the high magnitude caused by rapidly switching on and off the magnetic gradient

field during the DWI sequence. Eddy currents produce additional undesirable magnetic fields, which result in the geometric distortion of diffusion-weighted images and bring about a difference between the actual and prescribed local  $\mathbf{b}$ -matrix values. When eddy currents are present, individual DWIs become misaligned by shifting, mostly along the phase-encoded direction. The mean ADC image and the FA image derived from these misaligned images have artifacts such as increased anisotropy and blurring, especially in the periphery of the brain. These artifacts can be reduced through the use of well-designed pulse sequences, such as the bipolar diffusion-encoding gradients (Alexander *et al.*, 1997), and the pulse-sequence-specific preemphasis calibration (Papadakis *et al.*, 2000). Eddy-current artifacts can also be reduced by postprocessing schemes that are based on image registration. Image registration of the whole DWIs to a template (in general the  $B_0$  image) has been successfully applied as an eddy-current correction (Poupon *et al.*, 2000).

### 3. *Effects of Variations in Magnetic Susceptibility*

Adding an object with a locally heterogeneous magnetic susceptibility causes magnetic-field inhomogeneity and produces local magnetic-field gradients within the object. The magnetic-susceptibility variation in the brain adversely affects the DWIs because of the additional local gradients that behave like diffusion gradients. These may cause a spatially varying  $\mathbf{b}$ -matrix and may thus cause distortion in the DWIs. Furthermore, susceptibility inhomogeneity may result in a complete loss of signal. Susceptibility artifacts can easily be found at the regions adjacent to the sphenoid sinus or mastoid air, where a large difference between the air and tissues exists.

### 4. *Image Noise*

As is common in all MRI acquisitions, background noise degrades the true diffusion tensor. The noise level limits the maximal  $b$ -value. As the  $b$ -value increases to enhance contrast, the logarithm of the signal attenuation linearly decreases to the level of background noise, and the SNR is thus decreased. Moreover, background noise in DWIs biases tensor reconstruction and affects the degree of anisotropy by making isotropic structures appear anisotropic and by making anisotropic structures appear more anisotropic.

## C. PRACTICAL CONSIDERATIONS IN THE ACQUISITION OF DIFFUSION-TENSOR IMAGES

Diffusion-tensor-image acquisition is a balance between several factors, including SNR, spatial resolution, image distortion, and acquisition time. For example, a fast acquisition used to remove motion artifacts suffers from low

spatial resolution and other eddy-current effects. An increase in the spatial resolution deteriorates the SNR and thus requires repetitive scanning in order to increase the image quality. This, in turn, causes a longer acquisition time and increases the possibility of motion. Another method by which to increase the spatial resolution is to use a high-Tesla MRI, which allows us to acquire thinner slices with the same duration and similar SNRs. Unfortunately, MRIs with higher field strengths are more vulnerable to artifacts.

At present, single-shot spin-echo EPI is the most prevalent sequence for DTI, due to its fast acquisition speed and its insensitivity to motion artifacts. However, eddy currents, innately low spatial resolutions, and susceptibility artifacts continue to be limitations in the use of fast imaging sequences in DTI.

In conclusion, there is no method that yields the “best” diffusion-tensor images. Therefore, imaging sequences should be chosen according to research purposes on a case-by-case basis.

## VI. Visualization of Diffusion Tensors

In the previous sections, we discussed several scalar indices that quantify diffusion within a voxel. In this section, we will discuss various contrasting schemes of directional information about diffusion at each voxel. The directional information obtained from the diffusion tensor can be visualized by any of the following methods: (1) a color-coded vector map; (2) an arrow vector map; and (3) a three-dimensional tensor map.

### A. COLOR-CODED VECTOR MAPS

All natural colors can be represented by a mixture of three color components: red, green, and blue (RGB). Coincidentally, the principal direction of diffusion can be represented by the major eigenvector with three  $x$ ,  $y$ , and  $z$  components. Therefore, if we assign each color component to the component of the major eigenvector, we can easily visualize the direction of the eigenvector according to its color tone. For example, the component in the direction from the left to the right brain is assigned to red; the posterior-to-anterior direction is assigned to green; and the inferior-to-superior direction is assigned to blue (Fig. 12b). The color purely indicates the major direction of tissue structure. In cases where the major direction is parallel to the axis from the left ear to the right ear, as it is in the corpus callosum, the color will appear red. The cingulum bundle, located in the anterior–posterior direction, will have a green color. In the case of the major direction of 45 degrees with lateral superior orientation in the axial slice of the brain, as in the corona radiata, the color at the voxel will be an equal

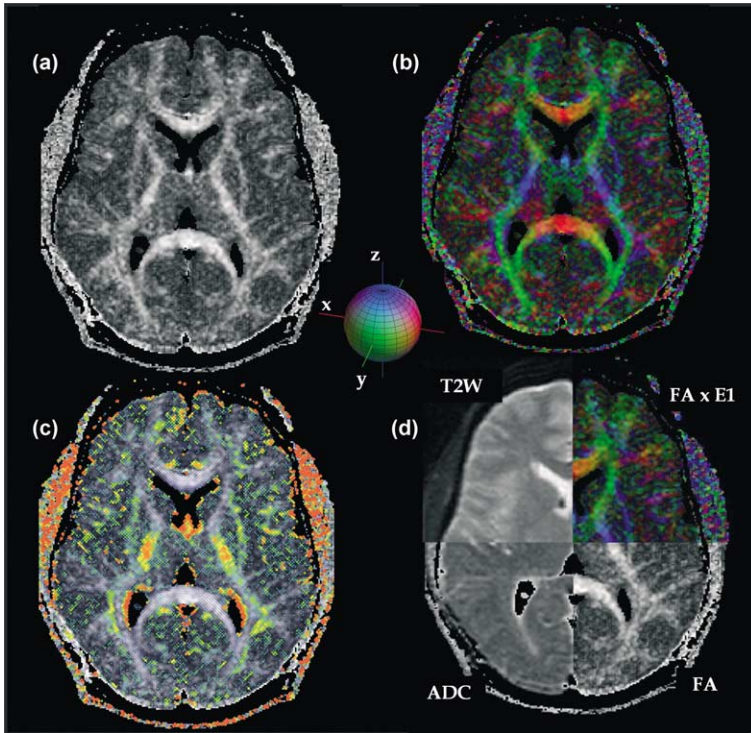


FIG. 12. Voxel-based visualization methods for the diffusion tensor. An axial slice of a diffusion-tensor image is displayed with the fractional anisotropy (FA) map (a), the color-coded vector map (b), the arrow vector map (c), and a combinatory display with T2, apparent diffusion coefficient (ADC), FA, and color-coded vector map ( $FA \times E1$ ) (d).

combination of red and blue, i.e., purple. It is possible to incorporate the anisotropy by multiplying RGB color values by FA and representing anisotropy by color brightness. Dark indicates lower anisotropy and bright indicates higher anisotropy at the voxel.

## B. ARROW-VECTOR MAP

Although the color-coding scheme provides the viewer with a good intuitive feel of the fiber directions at each voxel, it does not provide directional information that is precise enough to allow him or her to follow the fiber tracts visually. Another way of representing principal direction is the arrow-vector map. The major eigenvector can be resolved into in-plane components and out-of-plane



components. Arrows that have both orientation and length can represent in-plane components, which are 2D vectors. Out-of-plane components can be represented by color-scaled dots. For axial-slice images, we might see the following: the corpus callosum, where the in-plane component is dominant, can be mainly represented with an arrow, and the corona radiata in the PLIC, which has a dominant out-of-plane component, can be represented by hot color dots (Fig. 12c).

### C. THREE-DIMENSIONAL TENSOR MAPS

The two schemes of display introduced in Sections VI.A and VI.B are designed for use on a single vector field reduced from a tensor field. They do not provide shape information based on the second and third eigenvalues, and they may show changes in colors and arrows if the head position is not straight in the MRI coordinate. Because the diffusion tensor is modeled with an ellipse, the diffusion-tensor image can be better visualized by the display of an ellipse at each voxel. The three-dimensional rendering of an ellipse still captures the shape of the ellipse only ambiguously, however. We can partly overcome this ambiguity by displaying the tensor with a cube or a morphological mixture of line, plane, and sphere. Figure 13 shows an example of a tensor map that is displayed with ellipsoids and morphological objects.

## VII. Basics of Fiber Tractography

Although we can understand local fiber structures using voxel-based visualization, it is often difficult to follow the fiber tracts across the slices visually. Therefore, computerized fiber-tracking methods are needed to help one understand the fiber structures in three-dimensional space. The fiber-tracking algorithm virtually creates a trace of a particle by following the local fiber orientation as defined by the diffusion-tensor field. It is based on the assumption that local fiber orientation (for each voxel) is parallel to the major eigenvector of the diffusion tensor. A number of fiber-tracking algorithms have been developed (Basser *et al.*, 2000; Conturo *et al.*, 1999; Jones *et al.*, 1999; Mori *et al.*, 1999; Poupon *et al.*, 2000) since the introduction of DTI. In this section, we shall discuss the basics of the most prevalent fiber-tracking methods.

### A. CONTINUOUS TENSOR FIELDS

Fiber tracking can be obtained by our connecting each discrete voxel (currently on the order of  $2 \times 2 \times 2 \text{ mm}^3$ ) to the adjacent one in the principal

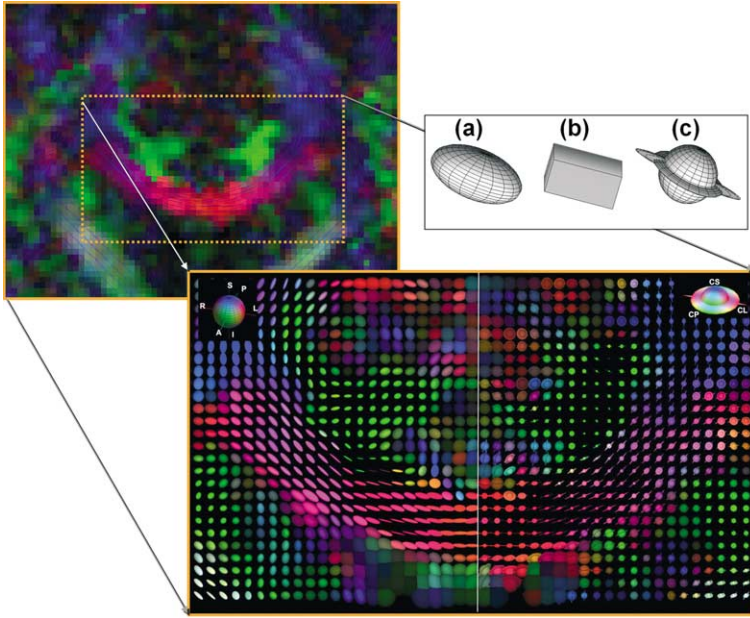


FIG. 13. Three-dimensional tensor map. A coronal section of the diffusion-tensor image can be displayed with a three-dimensional ellipsoid (a), a cubic object (b), and a geometric object (c). The zoomed figure shows the ellipsoidal display (left plane) and geometric-object display (right plane). The geometric objects are composed of lines, planes, and spheres according to the portion in the tensor of the linear, planar, and spherical components ( $c_l$ ,  $c_p$ , and  $c_s$ ).

direction given by the local diffusion tensor. Jumping from one voxel to the neighboring voxel, however, may result in nonsmooth and erroneous trajectories. To prevent the errors caused by discrete quantization of the tensor field, fiber tracking is generally conducted on the continuous representation of the tensor field. In the continuous tensor field, the trajectory and its tangent vector (i.e., the major eigenvector) can be calculated not only restrictedly at the regular discrete voxel but also anywhere in the three-dimensional continuous field, as shown in Fig. 14a. This can be accomplished through the interpolation of the tensor field using linear interpolation, Lagrange polynomials, or B-spline functions. The explanations in this section are all based on this continuous tensor field.

## B. BASIC STREAMLINE PROPAGATION

Fiber tracts can be computed by propagation of an anterograde and a retrograde streamline from an initial seed point in the direction of the major

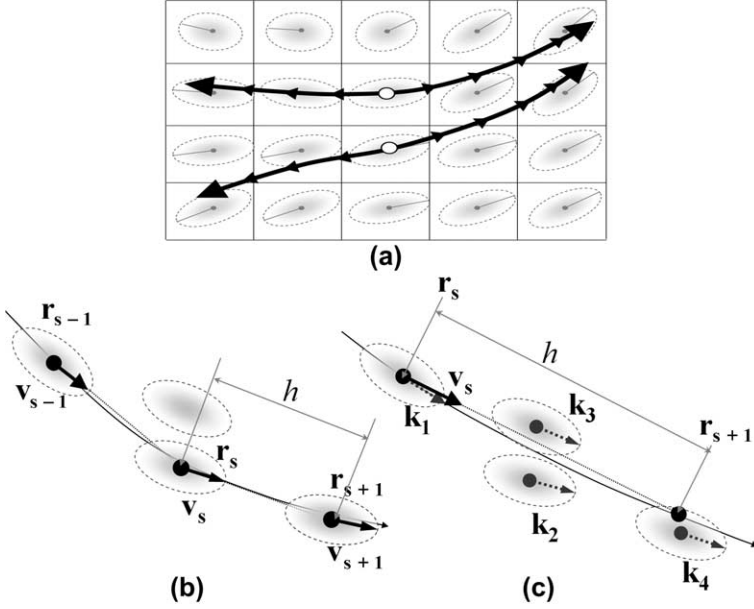


FIG. 14. The basic streamline algorithms in the continuous tensor field. From the seed point (the circle) in (a), fiber tracts are constructed in the anterograde and retrograde directions by following the principal direction of the diffusion vector. The propagation directions derived from major eigenvectors are calculated at any point in the continuous field (arrows in (a)), not restricted to a discrete voxel location such as the center of the voxel. The Euler algorithm (b) and the Runge–Kutta fourth-order algorithm (c) step for  $h$  distance in the propagation direction,  $\mathbf{v}_s$ . To decide the propagation direction  $\mathbf{v}_s$  at the point  $\mathbf{r}_s$ , the Euler algorithm utilizes the major eigenvector at  $\mathbf{r}_s$ , whereas the Runge–Kutta fourth-order method utilizes four major eigenvectors from four trial points ( $\mathbf{k}_1$ ,  $\mathbf{k}_2$ ,  $\mathbf{k}_3$ , and  $\mathbf{k}_4$ ). This reduces the accumulation errors that appear in Euler’s method when the step size is big.

eigenvector for a small spatial step. The points on the trajectory  $\mathbf{r}(s)$  can be derived by

$$\frac{d\mathbf{r}(s)}{ds} = \mathbf{v}(s) \quad (18)$$

where  $\mathbf{v}(s)$  is a unit tangent vector to  $\mathbf{r}(s)$  at the time  $s$ . With the initial condition,  $\mathbf{r}(s=0) = \mathbf{r}_0$ , called the seed point, the solution for this differential equation can be derived by an iterative process:

$$\mathbf{r}_{s+1} = \mathbf{r}_s + h \cdot \mathbf{v}_s \quad (19)$$

where we calculate the next propagation location  $\mathbf{r}_{s+1}$  by adding to the current location  $\mathbf{r}_s$  the displacement with step size  $h$  along the propagation direction  $\mathbf{v}_s$ . A

complete trajectory path from the initial seed point  $\mathbf{r}_0$  can be defined with two sets of points in the anterograde propagation (i.e., where  $\mathbf{e}_1$  is the major eigenvector of the tensor at  $\mathbf{r}_0$ ) and the retrograde propagation (i.e.,  $\mathbf{v}_0 = -\mathbf{e}_1(\mathbf{r}_0)$ ).

### 1. The Euler Method and the Runge-Kutta Method

The simplest algorithm for solving our differential equation (Eq. 19) is the Euler method, which utilizes the major eigenvector as the propagation direction (Fig. 14b):

$$\mathbf{r}_{s+1} = \mathbf{r}_s + h \cdot \mathbf{e}_1(\mathbf{r}_s) \quad (20)$$

where  $\mathbf{e}_1(\mathbf{r}_s)$  is the major eigenvector at point  $\mathbf{r}_s$ . However, the Euler method can suffer from large accumulated errors unless the step  $h$  is small enough to prevent the error.

The most well-known integration solver is the fourth-order Runge-Kutta method. To obtain the propagation direction,  $\mathbf{v}_s$ , four tangent vectors at neighboring points are evaluated, as in Fig. 14c: once at the initial point, twice at the trial midpoints, and once at the trial endpoint (Press *et al.*, 1992; Tench *et al.*, 2002).

$$\mathbf{v}_s = \frac{1}{6}(\mathbf{k}_1 + 2\mathbf{k}_2 + 2\mathbf{k}_3 + \mathbf{k}_4) \quad (21)$$

where

$$\begin{aligned} \mathbf{k}_1 &= \text{sign}(\mathbf{v}_{s-1} \cdot \mathbf{e}_1(\mathbf{r}_s))\mathbf{e}_1(\mathbf{r}_s), \\ \mathbf{k}_2 &= \text{sign}(\mathbf{v}_{s-1} \cdot \mathbf{e}_1(\mathbf{r}_s + h/2 \cdot \mathbf{k}_1))\mathbf{e}_1(\mathbf{r}_s + h/2 \cdot \mathbf{k}_1), \\ \mathbf{k}_3 &= \text{sign}(\mathbf{v}_{s-1} \cdot \mathbf{e}_1(\mathbf{r}_s + h/2 \cdot \mathbf{k}_2))\mathbf{e}_1(\mathbf{r}_s + h/2 \cdot \mathbf{k}_2), \\ \mathbf{k}_4 &= \text{sign}(\mathbf{v}_{s-1} \cdot \mathbf{e}_1(\mathbf{r}_s + h\mathbf{k}_3))\mathbf{e}_1(\mathbf{r}_s + h\mathbf{k}_3) \\ \text{sign}(x) &= \begin{cases} 1, x > 0 \\ -1, x < 0 \end{cases} \end{aligned} \quad (22)$$

where  $\mathbf{e}_1(\mathbf{r}_s)$  is the major eigenvector at the position of  $\mathbf{r}_s$  and  $\mathbf{v}_{s-1}$  is the propagation direction in the previous step. Sign function is used to align the vectors  $\mathbf{k}_1$ ,  $\mathbf{k}_2$ ,  $\mathbf{k}_3$ , and  $\mathbf{k}_4$  at four trial points in the direction of the propagation, since the major eigenvector at the tensor calculation may arbitrarily have either a forward or a reverse direction.

### 2. Termination Criteria of Propagation

The streamline propagation iteratively continues until it reaches outside white matter defined by the termination criteria. For example, the propagation stops where the anisotropy is lower than the threshold, which is regarded to be the anisotropy at the boundary between white matter (high anisotropy) and gray matter (low anisotropy). The rapid change in the propagation direction is also

often used as a termination criterion due to the limited amount of curvature of trajectory per spatial increment in the physiology. However, the criterion of low anisotropy may mistakenly lead the propagation algorithm to stop at a fiber-crossing region that shows a low anisotropy, or to stop near subcortical gray matters that have relatively well-organized fibers but show low anisotropy. To overcome this mis-stopping problem, a stopping mask drawn on the structural MRI or a termination criterion based on the uncertainty of the diffusion direction (Behrens *et al.*, 2003) can be used.

### C. PROBLEMS IN FIBER TRACTOGRAPHY

Fiber tractography, especially that based on streamline propagation, suffers from two major types of problems: partial volume effects and noise effects. We shall discuss these problems and several methods used to overcome them.

#### 1. *Partial Volume Effects in Fiber Tracking*

The basic assumption of tractography is that the principal direction of diffusion aligns with a single fiber orientation. This may not be especially true for low spatial resolution (about  $2 \times 2 \times 2 \text{ mm}^3$ ) in the current system. Several tissue structures, such as two different pathway fibers, may lie within a specific voxel and contribute to form a single tensor at the voxel. Since the axonal diameter is on the order of  $10 \text{ }\mu\text{m}$ , the partial volume effect may not be easily overcome, despite progress in MRI techniques. We will discuss in detail the partial volume effect seen in fiber tracking.

*a. Ambiguity of the White-Matter Boundary.* The voxels located at the boundaries between white-matter fiber tracts and neighboring structures are typical examples of areas affected by the partial volume effect (Fig. 15a). The anisotropy of a voxel at this boundary is generally reduced in proportion to the amount of nonfiber structure. The orientation of the diffusion in this region is very susceptible to noise and to surrounding structures.

*b. Fiber Crossing.* The fiber crossings are easily found in the human brain; they include the regions between the corona radiata and radiation of the corpus callosum, between the corticospinal tracts and the pontocerebellar fibers, etc. (Wiegell *et al.*, 2000). The diffusion tensor at these crossing fibers tends to show increased planar or spherical components of diffusion and reduced anisotropy (Fig. 15b). In this region, the principal direction of diffusion is very sensitive to noise, and the ambiguity of the propagation direction is augmented. To overcome the ambiguity due to fiber crossing in tracking, several schemes for regularizing propagation have been developed by incorporation of the inertia term of the previous propagation with the current tensor. This method will be discussed in Section VII.D.

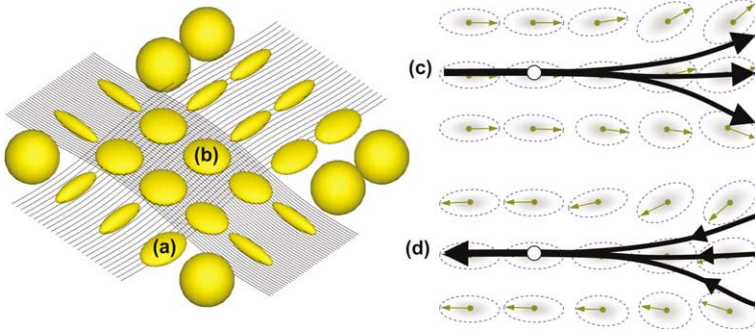


FIG. 15. Partial volume effects on the diffusion tensor. A tensor at the boundary of the fibers and nonfiber structures (a) and a tensor where two fiber bundles cross have highly augmented ambiguity. At the diverging fibers, the streamline approach cannot explain fiber branching from a single point to several fibers (c). Instead, fiber branching can be explained by the merging of multiple fibers starting from multiple seed points (d).

*c. Fiber Branching.* For a streamline approach, it is difficult to represent fibers diverging from a single streamline starting at a location in the region of interest (ROI). This fiber-branching problem can be partly solved if we merge two separate fibers instead of splitting one fiber into two separate fibers, as in Fig. 15d. Practically, this can be implemented by reconstructing all the brain fibers with seed points at the voxels in the entire white matter and choosing fibers that penetrate a specific ROI.

## 2. Noise and Fiber Tracking

Fiber tracking is very sensitive to noise in the tensor field, which might be generated from acquisition artifacts. A slight deviation of the major eigenvector due to noise and its accumulation will cause severe changes in the trajectory. Therefore, reducing noise and regularizing the tensor field are critical for reliable fiber tracking.

One basic approach is to use general image-filtering methods. Gaussian filtering can be used to remove random Gaussian noises in DWIs. However, Gaussian filtering degrades spatial resolution and causes image blurring. Nonlinear anisotropic smoothing (Parker *et al.*, 2000) is designed to remove high-frequency noise while preserving the boundaries of structures of interest.

Another approach is to utilize *a priori* knowledge of the fiber tracts in regularizing the tensor field on which the fiber tracking is performed. The regularization of the tensor field is based on the global properties of the fibers, such as the limited curvature of the fiber trajectory. Spline-based approximation of the tensor field (Basser *et al.*, 2000) is one of the simple methods of

incorporating the *a priori* hypothesis of limited curvature. A global restoration technique using the Bayesian framework (Poupon *et al.*, 2001) is another example that utilizes the low-curvature information in the regularization. The optimal direction map is a tradeoff between the bending energy of trajectories and their faithful following of the measured diffusion-tensor field. Instead of using eigenvectors directly derived from the original tensor field, fiber tracking is performed on regularized direction maps.

#### D. REGULARIZED STREAMLINE ALGORITHMS

As discussed before, a straightforward implementation of eigenvector-tracking streamline algorithms has an ambiguity problem at locations where propagation faces fiber crossing. To overcome this problem, advanced streamline algorithms have regularized this propagation. The propagation vector,  $\mathbf{v}_s$  in Eq. (19), is an outgoing vector from the current tensor at location  $\mathbf{r}_s$ , while  $\mathbf{v}_{s-1}$ , the propagation direction at previous step  $\mathbf{r}_{s-1}$ , is an incoming vector to the current tensor, denoted as  $\mathbf{D}$ . The regularization scheme is to derive the outgoing vector  $\mathbf{v}_s$  by modulating the incoming vector  $\mathbf{v}_{s-1}$  with the current tensor matrix  $\mathbf{D}$ .

Westin and colleagues (2002) suggested a projection method in which the outgoing vector is derived by projection of the incoming vector onto a tensor matrix operated with a tensor mapping function  $F$ , as demonstrated below:

$$\mathbf{v}_s = F(\mathbf{D}) \cdot \mathbf{v}_{s-1} \quad (23)$$

One example of the tensor projection operation is to use the geometric tensor matrices, i.e.,  $\mathbf{D}_b$ ,  $\mathbf{D}_p$ , and  $\mathbf{D}_s$ , and the geometric index, i.e.,  $c_b$ ,  $c_p$ , and  $c_s$  of the tensor  $\mathbf{D}$  from Eq. 14, as below:

$$F(\mathbf{D}) = \begin{cases} c_l \mathbf{D}_l, & \text{if } c_l > c_p, c_s, \\ c_p \mathbf{D}_p, & \text{if } c_p > c_l, c_s, \\ c_s \mathbf{D}_s, & \text{if } c_s > c_l, c_p, \end{cases} \quad (24)$$

The tensor line method, also called the tensor deflection method (TEND) (suggested by Weinstein *et al.* [1999]), combines the incoming vector  $\mathbf{v}_{s-1}$ , the projected vector, and the major eigenvector of the current tensor  $\mathbf{D}$  to determine the outgoing vector,  $\mathbf{v}_s$ .

$$\begin{aligned} \mathbf{v}_s &= f \mathbf{e}_1 + (1-f) \{ ((1-g) \mathbf{I} + g \mathbf{D}) \cdot \mathbf{v}_{s-1} \} \\ &= f \mathbf{e}_1 + (1-f) \{ F(\mathbf{D}) \cdot \mathbf{v}_{s-1} \} \end{aligned} \quad (25)$$

where the line components  $c_l$  are used as a controlling variable  $f$ .

Both the tensor projection method and the tensor line method have the tensor mapping function  $F$ , which deflects the incoming vector towards the major eigenvector direction of  $\mathbf{D}$  but limits the curvature of the deflection, as illustrated in Fig. 16a. When the diffusion is isotropic,  $c_l$  becomes zero,  $F(\mathbf{D})$  equals a scaled identity matrix, and the outgoing vector is the continuation of the incoming vector, i.e.,  $\mathbf{v}_s = \mathbf{v}_{s-1}$ . The continuation of the incoming vector also occurs when the incoming vector is parallel to the plane spanned by two eigenvectors  $\mathbf{e}_1$  and  $\mathbf{e}_2$ , which correspond to the two largest eigenvalues.

The streamline algorithm with a regularization scheme is very efficient at penetrating ambiguous tensors, as shown in Fig. 16b. However, the regularized streamline algorithm may not correctly follow the fibers that have high curvature, due to the effect of the inertia component in tracking. Neither does it have a method to differentiate between fiber crossing and fiber kissing (i.e., the pattern of fibers diverging after drawing close to each other) in a voxel. In this situation, we should decide whether to stop, to rapidly turn the propagation direction, or to continue using regularization.

Figure 17 summarizes the procedure of fiber tracking discussed in this section. The extraction of fibers of interest from constructed fibers will be discussed in Section IX.C. Figure 18 shows a result of fiber tractography

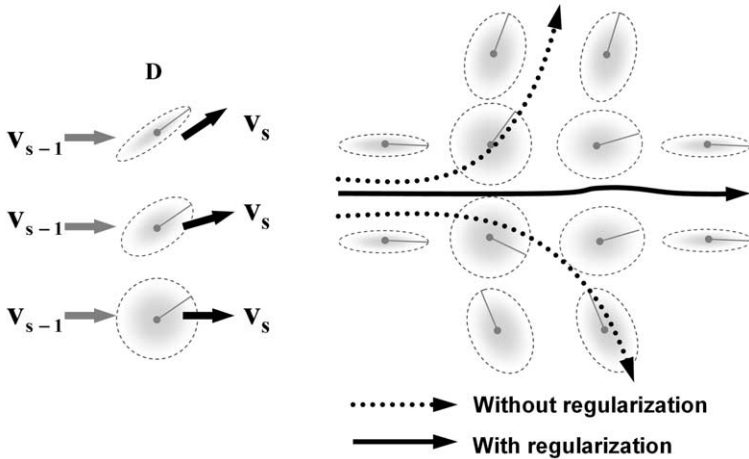


FIG. 16. The regularized streamline approach. When multiplied with the anisotropic diffusion tensor  $\mathbf{D}$ , the incoming vector  $\mathbf{v}_{s-1}$  is deflected towards the major eigenvector direction,  $\mathbf{D}$ . When the tensor  $\mathbf{D}$  is isotropic,  $\mathbf{D}$  is equal to the identity matrix and the propagation continues toward the incoming vector, i.e.,  $\mathbf{v}_s = \mathbf{v}_{s-1}$  (a). When a streamline faces a tensor close to isotropic, the ambiguity is increased, and it may propagate in the wrong direction. Under regularization, the streamline can penetrate the ambiguous tensors in the direction of the previous propagation (b).



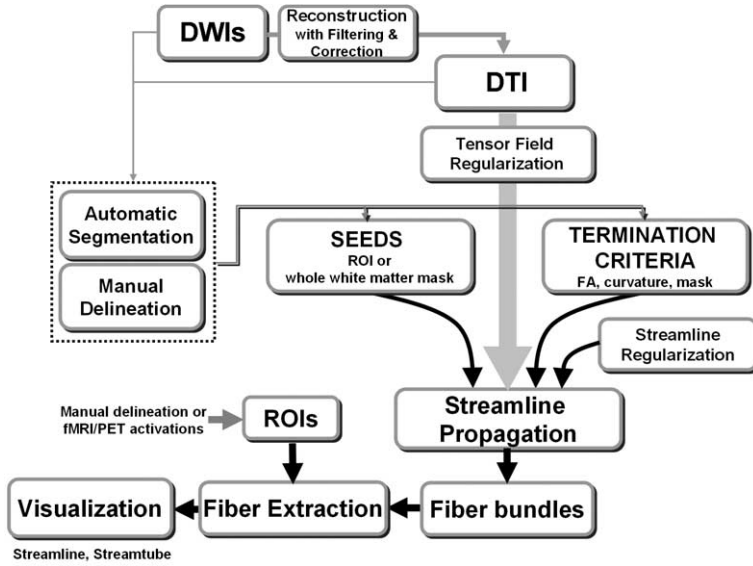


FIG. 17. A diagram of general fiber tractography. General fiber tractography is based on a streamline technique that requires seed points, termination criteria, and an integration solver, i.e., a streamline propagation mechanism. Seed points can be assigned by manual delineation of regions of interest or by generation of a white-matter mask from a segmentation algorithm. Fractional anisotropy and curvature changes are often used as the termination criteria. From the reconstructed fibers, fibers of interest can be extracted; this is explained in detail in [Section IX.C](#).

reconstructed using the Runge–Kutta fourth-order algorithm with seed points of the entire white matter.

## VIII. Advances in Fiber Tractography

### A. CONNECTIVITY MAPPING

The streamline techniques are deterministic in the sense that they utilize the eigenvector field reduced from the tensor field and do not allow for uncertainty of fiber direction. In the streamline technique, therefore, there is no mechanism to evaluate how reliably the path represents the true pathway or to evaluate how much more probable the connectivity from a seed point to a certain point is, compared to any other certain point. More recent approaches are statistical in nature and take

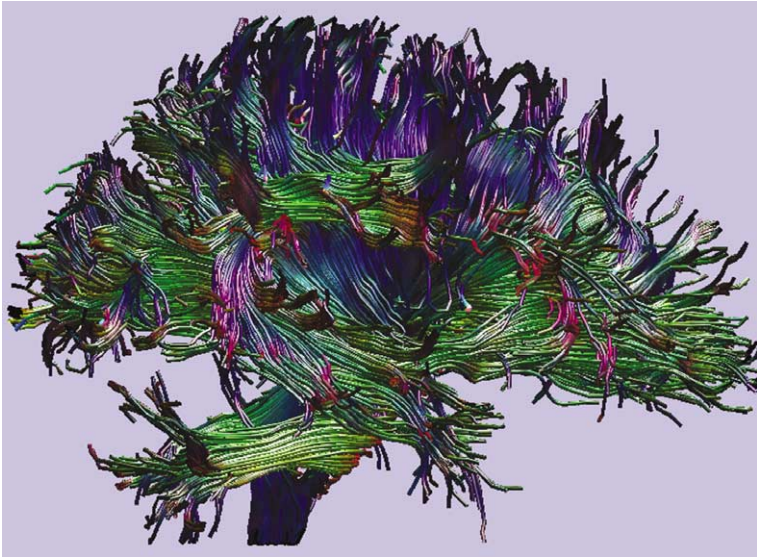


FIG. 18. Whole-brain fiber bundles in lateral view. The whole-brain fiber bundles are reconstructed using the fourth-order Runge-Kutta algorithm with seed points in the whole white matter. The diffusion-tensor image is acquired from 3-Tesla GE Echospeed systems using a line-scan diffusion-imaging sequence (LSDI). The fiber tractography was conducted using the DoDTI (<http://neuroimage.yonsei.ac.kr/dodti>).

into consideration all of the diffusion information with the assumption that the probability of a fiber's propagating in a given direction is proportional to the corresponding diffusion coefficient. In contrast to the streamline approach, which is a one-to-one mapping, all connectivity-mapping approaches have in common that a single initial seed can have multiple end-points or a probability map, which makes it possible to evaluate the relative connectivity between the regions.

#### 1. *Fiber Tractography by Solution of the Diffusion Equation*

One way to understand diffusion data is to spread a virtual concentration peak of heat by the law of diffusion, which can be formulated with partial differential equations (PDEs). We can achieve fiber tractography by solving PDEs where the diffusion coefficients of the heat equation equal the diffusion coefficients of the diffusion tensor. The solution can be obtained by iterative simulation of a peak concentration as it diffuses inside the brain based on the heat equation alone (Gembris *et al.*, 2001) or based on the heat equation with a convection term, to enhance the anisotropy of the diffusion equation (Batchelor *et al.*, 2002).

## 2. Fast-Marching Tractography

The fast-marching tube (Parker *et al.*, 2002) is a front propagation method wherein the interface or front propagates in the direction of high driving speed. The variable rate of the propagation is governed by the directionality of the tensor. In the direction of the major eigenvector,  $\mathbf{e}_1$ , the front propagates faster than the direction of the other two eigenvectors,  $\mathbf{e}_2$  and  $\mathbf{e}_3$ . The front, started at a seed point, will cross regions in the brain at different times, and this generates a map of the arrival time at all points in the brain from the seed point. From this arrival-time map, we can calculate the path of connection from a seed point to any point in the volume by finding the minimum cost path back to the seed point from that point. Although this method is performed on the eigenvector field as the streamline approach is, its one-to-many mapping is the element that provides the evaluation of relative connectivity. Figure 19 shows an example of this fast-marching tractography (FMT).

## 3. The Monte Carlo Random-Walk Simulation

During the diffusion process, a particle performs a random walk through the medium. A Monte Carlo random-walk simulation (Hagmann *et al.*, 2003; Koch *et al.*, 2002) is based on this particle phenomenon with a local transition probability. The probability of transition in a given direction is chosen depending on the local diffusion coefficient along the propagation direction. The particle moves

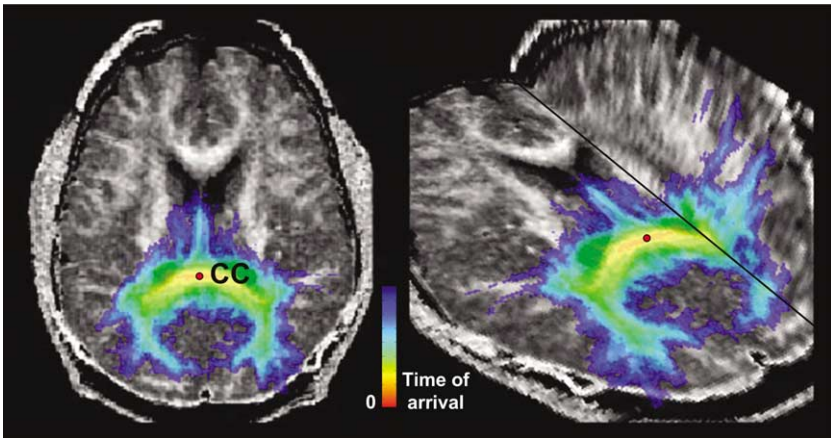


FIG. 19. Connectivity mapping using fast-marching tractography. A time-of-arrival map is derived using fast-marching tractography from a seed point located in the middle of the corpus callosum. In contrast to streamline approaches, fast-marching tractography has one-to-many mapping that makes it possible to evaluate the relative connectivity between the pairs of points in the brain.

for a short time by stepping along a random direction, which is determined according to the transition probability at the initial location. In each iterative step, a new direction is randomly sampled and the new transition-probability distribution is determined by the diffusion tensor at each location. Toward the new direction, the virtual particle propagates with a diffusivity corresponding to the direction. Particles will move with a higher probability when traveling along the fiber direction than when they travel perpendicular to it. In a number of such random walks starting from a region, the frequency that some other region has been reached can be used as a relative measure of the anatomical connectivity between the two regions.

In order to constrain the random-walk process with the global properties of the fiber trajectory, hybrid approaches have been designed in order to find the optimal path between a pair of regions by combining the *a priori* information on the path curvature with the information from the diffusion-tensor data (Hagmann *et al.*, 2003).

#### 4. *The Probabilistic Approach Using Uncertainty*

In general, analysis of the diffusion tensor has involved the fitting of a local diffusion model to the diffusion-weighted data at each voxel. It is based on the assumptions that the local diffusion profile is Gaussian and that the parameters of Gaussian diffusion are completely known. However, uncertainty exists in the relationship between the diffusion measurements and the underlying fiber structures. Noise in the NMR signal (both physical and physiological) can be one source of this uncertainty. Behrens and colleagues (2003) presented a method for the treatment of these uncertainties. They formulated the local uncertainty in the parameters of the generative diffusion model at a voxel level, in the form of posterior probability density functions on these parameters. Global connectivity is based on the probabilistic tractography, which incorporates every possible fiber orientation at every voxel with the probability given by the measured diffusion-tensor data.

## B. HIGH-ANGULAR-RESOLUTION DIFFUSION IMAGING

In the previous sections, we have discussed the methods for enhancing the reliability of fiber tracking, especially in the case of the partial volume effect in terms of the postprocessing methodology. These techniques are mostly based on the assumption of a simple Gaussian diffusion on a voxel. However, with a Gaussian tensor model, it can be difficult to describe the fiber architecture in voxels where multiple directional fibers coexist. As discussed in the previous section, several regularization techniques on the traditional diffusion-tensor data

have been designed to solve mixtures of multiple fiber directions. However, they may fail in cases of high curvature, as in the arcuate fascicles near the cortex. The problem of fiber crossing can be solved using high-angular-resolution diffusion imaging (HARD), in which over a hundred directional diffusivities evenly spaced out in a three-dimensional space are measured to generate a diffusion displacement profile. This diffusion displacement profile does not require any *a priori* knowledge of the diffusion characteristics of the structure. Several methods have been proposed for measuring HARD techniques. These include multitensor modeling (Tuch *et al.*, 2002), diffusion-spectrum imaging (Tuch *et al.*, 2002), and Q-ball imaging (Tuch, 2004; Tuch *et al.*, 2003). HARD is used to analyze multiple fiber bundles within a voxel (Frank, 2002). These imaging techniques have been receiving growing amounts of attention. However, the disadvantage of HARD techniques is that they are computationally intensive, and require a much greater acquisition time than is necessary for general tensor acquisition. Figure 20 shows an example of the Q-ball imaging method about the optic radiation.

## IX. Quantification of White Matter using DTIs

Quantitative evaluation of the white matter benefits from the fact that the diffusion of water molecules in white-matter tissues is affected by the properties of neuronal fibers and their surrounding structures. The quantification of diffusion-tensor data for investigations of white matter has generally been approached using the following methods: (1) ROI-based methods; (2) voxel-based methods; and (3) fiber tractography-based methods.

### A. ROI-BASED ANALYSIS OF DTIs

ROI methods begin by identifying anatomical brain regions and comparing the anisotropy or the extent of the region. Due to its relatively easy accessibility, this method has been a basic tool in many researches using DTI (Kubicki *et al.*, 2003; Peled *et al.*, 1998). The ROI-based approach, however, requires *a priori* hypotheses to predefine the expected ROI. Therefore, ROIs are often chosen at the major fiber bundles that are relatively easy to separate from other structures. Since the boundary of a specific fiber bundle is not clear and a single voxel may contain multiple types of fibers due to the low spatial resolution of the diffusion-tensor image, care should be taken to ensure the consistent measurement of the ROI.

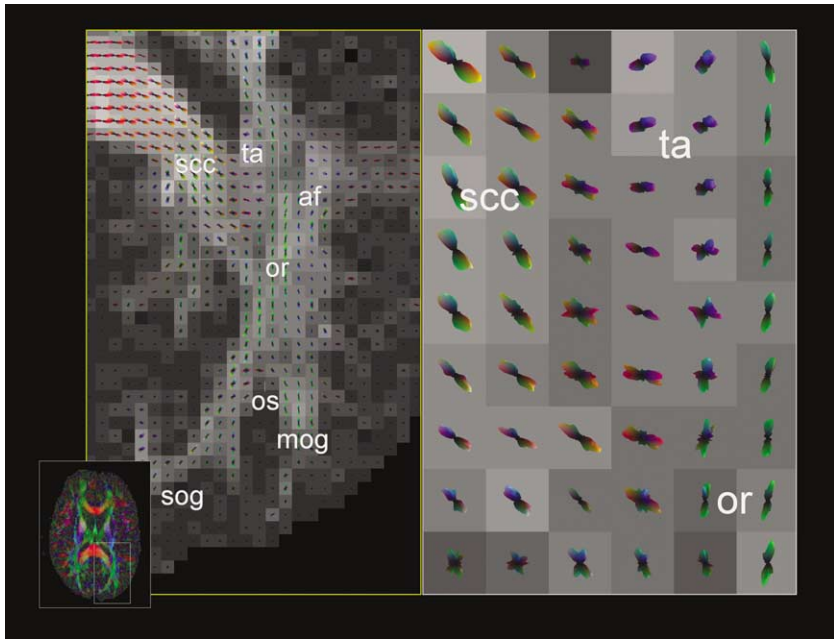


FIG. 20. Q-ball diffusion image (QBI) of three-way fiber crossing between the splenium of the corpus callosum, the tapetum, and the optic radiation. The QBI data were acquired on a 3-Tesla Siemens Trio with  $b = 4000 \text{ s/mm}^2$ , 252 directions, and 2.2-mm isotropic resolution. af, arcuate fasciculus; mog, middle occipital gyrus; or, optic radiation; os, occipital sulcus; scc, splenium of corpus callosum; sog, superior occipital gyrus; ta, tapetum. Courtesy of David S. Tuch, Harvard Medical School. Adapted from [Tuch \(2004\)](#) with permission of Wiley-Liss, Inc., a subsidiary of John Wiley & Sons, Inc. © 2004 Wiley-Liss, Inc.

## B. VOXEL-BASED STATISTICAL PARAMETRIC MAPPING OF DTIS

A voxel-based strategy is more exploratory and is suitable for identifying unanticipated or nonhypothesized areas of abnormal white-matter morphology. Voxel-based methods have also been used for studies where the ROI of potential abnormality is difficult to define precisely. The process for voxel-based quantification of diffusion tensors is basically similar to that for functional images such as fMRI or positron emission tomography (PET). The basic and critical requirement for voxel-based analysis is to perform spatial normalization with high reliability in order to minimize anatomical factors in the evaluation of the features of interest, such as FA and mean ADC. This spatial normalization is usually performed by spatial transformation of individual images to a template space, a process often called image registration. A template, which plays an important role inasmuch as it provides a standard space for the individual brains,

is generally chosen to represent the group being tested; for example, a template could be a group-averaged image.

In general, a T2-weighted image acquired on the same scan with the diffusion-tensor image or non-diffusion-weighted reference image is used to estimate the nonlinear transformation function to a template. With this function, diffusion-parameter images (e.g., FA and mean ADC) are transformed to the template space. However, T2-weighted images do not include information essential for finding anatomical correspondences to the underlying white-matter structures (namely, the fiber tract's orientation and organization), and thus may not be appropriate for finding precise anatomical correspondences in DTI. [Park and colleagues \(2003\)](#) showed that registration using the whole tensor information yields better registration performance than just using an FA image or T2-weighted image in the registration of diffusion tensor images.

### C. FIBER TRACTOGRAPHY-BASED ANALYSIS OF DTIs

White matter is a connectional architecture that cannot be fully described by a single voxel, and the most meaningful representations of fiber organization are obtained in terms of fiber bundles. Therefore, it is appropriate to evaluate the fiber bundles to increase the specificity of DTI.

It is of great importance to define and extract fibers of interest (FOIs) with high reliability in the analysis of fibers. The simplest way of generating FOIs is to perform fiber tracking starting at the seed points in the ROI drawn on the slices of the T2-weighted image or FA image. Another way of extracting FOIs is based on the whole-brain fiber bundles reconstructed from the seed points at the whole white matter. Among the reconstructed fiber of the entire brain, fibers that penetrate the ROI are selected as fiber bundles of interest. This method is particularly advantageous when branching occurs.

The group of fibers reconstructed from an ROI may contain unwanted fibers, including various directional fibers, due to the initial value sensitivity of fiber tracking. For example, by drawing an ROI at one or more than one slice of the PLIC, the corticospinal tract cannot be separated well enough from the fibers connecting the other cortical regions through the PLIC. This is because the subtypes of fibers in the PLIC that connect various cortical regions cannot easily be identified on the image slices. To emphasize the fibers that are of concern, researchers often use two or more ROIs to exclude fibers that started at the same ROI but ended at a different brain region. The example of FOI derived using multiple ROIs are displayed in [Fig. 21](#). The parcellation of cortical gray matter using high-resolution structural MRI may be useful for the identification of fiber bundles, since the fiber bundles are interconnecting cortical regions in addition to



interconnecting the cortex with the subcortical structures. Figure 22 shows an exemplary usage of cortical parcellation in identifying the fibers that originated from the right precentral gyrus (Park *et al.*, 2004).

A fiber bundle allows us to measure the anisotropy index, such as the mean FA of the particular fiber bundle as well as its size and shape. We can think of several ways of quantifying the extracted fiber bundles. The mean values of fiber characteristics such as anisotropy and cross-sectional area along the fiber bundles can be used for the statistical evaluation. The profile of anisotropy or cross-sectional area along the fibers can also be clinically important. However, the absolute number of axons connecting two cortical regions can hardly be calculated from tractography, because each streamline of the tractography represents a gross fiber bundle containing thousands or more of the axonal fibers, depending on the voxel size and anatomical location. Therefore, the number of fiber bundles reconstructed by current tractography may not be a direct index of the anatomy of the brain.

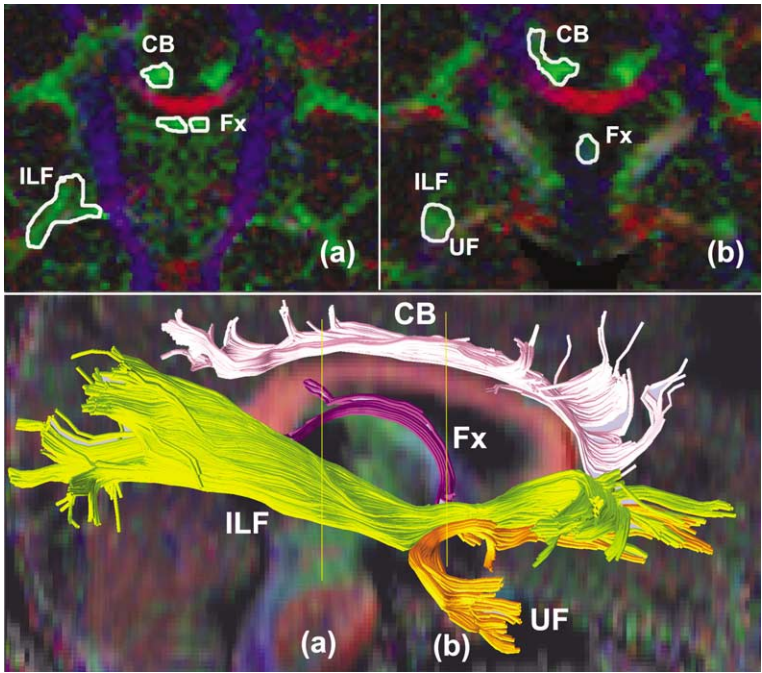


FIG. 21. Fibers of interest. The cingulum bundle (CB), inferior longitudinal fascicle (ILF), uncinate fascicle (UF), and fornix (Fx) are derived from multiple regions of interest delineated at two separate coronal slices.



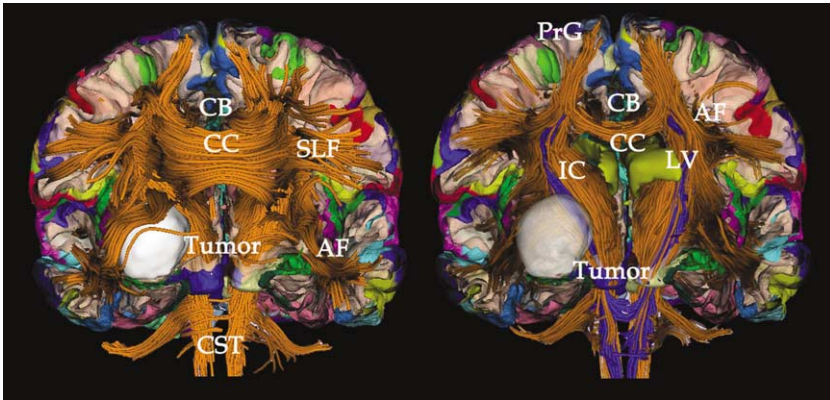


FIG. 22. Fiber tractography in tumor surgery. Fiber tractography can be used in the surgical planning for a tumor surgery. The left panel shows the tractography of the entire brain displayed with cross-sections of gray- and white-matter surface. The right panels show the fibers (in blue) that originated from the right precentral gyrus (blue color in cortex) and are located closest to the tumor. CC, corpus callosum; SLF, superior longitudinal fasciculus; CB, cingulum bundle; AF, arcuate fibers; IC, internal capsule; CST, cortico-spinal tract; PrG, precentral gyrus; LV, lateral ventricle. Adapted from [Park \*et al.\* \(2004\)](#) with permission from the American Society of Neuroradiology.

#### D. PRACTICAL CONSIDERATIONS IN THE ANALYSIS OF DTIS

One of the most important issues in the analysis of diffusion-tensor images is the interpretation of findings, especially for studies that use the anisotropy index. Since the meaning of macroscopic anisotropy is affected by the many factors discussed earlier, it may not be correct to simply state that the difference of FA indicates the difference or abnormality in the connectivity. To reduce the complexity in the interpretation of the anisotropic difference, it will be helpful to reference other imaging techniques. For example, the magnetization transfer ratio, which is sensitive to the myelination, can be used to investigate the portion of anisotropy that is due mainly to either the cell type of the fiber or the structural coherence of fibers.

Exploration of fiber properties by fiber tractography requires great care in interpretation as well, since there are many considerations, not the least of which is the problem of how to evaluate fibers that cross. The fiber trajectories generated by following the largest and the most homogeneous fiber bundles cannot represent a diameter that is much smaller than the size of a voxel. If we can achieve a more reliable white-matter tractography, this will be an important step towards the quantification of fiber bundles of concern, which would lead to a further understanding of “neural connectivity.”

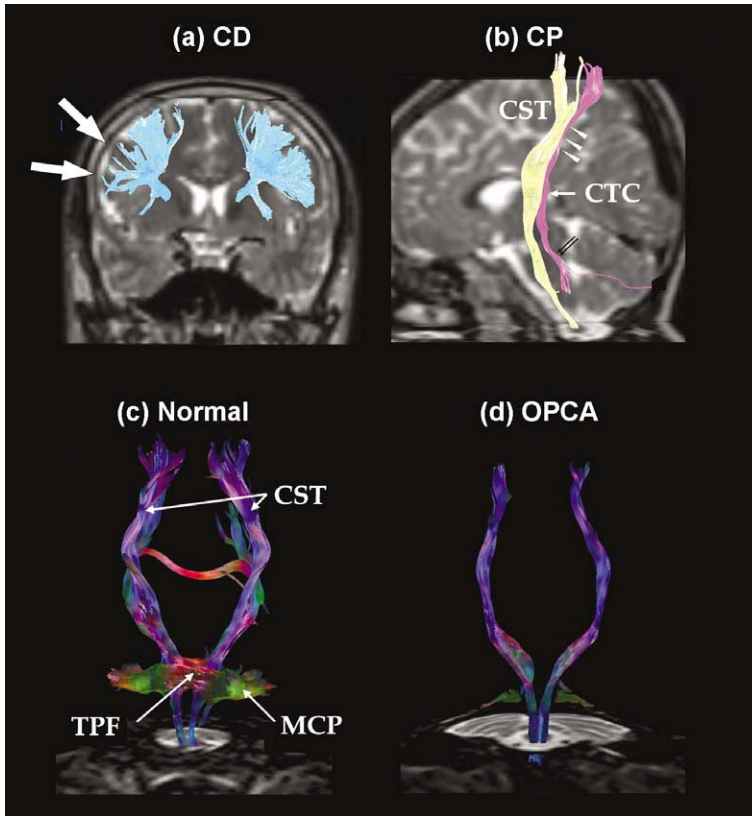


FIG. 23. Clinical applications of fiber tractography. A patient with cortical dysplasia (CD) shows reduced subcortico-cortical white-matter connectivity (a). In a cerebral palsy (CP) patient, the sensory fibers are reduced but motor fibers are normal (b). In a patient with olivopontocerebellar atrophy (OPCA), transverse pontine fibers (TPF) and the middle cerebellar peduncle (MCP) are reduced or absent (d); compare with the normal subject (c). CST, corticospinal tract; TPF, transverse pontine fibers; CTC, cortico-thalamic connection. Courtesy of Seung-Koo Lee, Department of Diagnostic Radiology, Yonsei University.

## X. Applications of DTI

Alteration of molecular mobility due to changes in structures, properties, or tissue compartments can affect the diffusion tensor; some examples include inflammation, demyelination, axonal loss and reorganization, cytotoxic edema, and infiltration of white-matter fibers by tumor. The clinical applications of DTI based on these white-matter pathologies include brain ischemia, trauma, tumor, focal epilepsy, multiple sclerosis, Alzheimer's disease, and schizophrenia. DTI has also been used for normal-development studies and aging studies. Most of

these research projects have been conducted by exploring the geometry and the degree of anisotropy of the diffusion. There are many recent reviews that deal with specific cases (Dong *et al.*, 2004; Jellison *et al.*, 2004; Kubicki *et al.*, 2002; Neil *et al.*, 2002; Sullivan and Pfefferbaum, 2003; Sundgren *et al.*, 2004; Taylor *et al.*, 2004). As the anisotropic diffusion in white matter renders estimation of fiber tracts, diffusion tensors provide information on the connectivity between the regions using fiber tractography. Application areas of fiber tractography have been expanded gradually, and the usefulness of fiber tractography has been validated in some areas. As shown in Fig. 22, fiber tractography can be applied to explore the effect of tumors or space-occupying lesions on the white-matter architecture, and discoveries about these effects can be used in surgical planning (Clark *et al.*, 2003; Mori *et al.*, 2002; Park *et al.*, 2004). This method can be useful in many clinical applications, including central-nervous-system neoplasm (Melhem *et al.*, 2002), white-matter diseases such as cerebellar degeneration (Lee *et al.*, 2003) and Wallerian degeneration (Pierpaoli *et al.*, 2001), and pediatric brain abnormalities such as congenital anomalies (Lee *et al.*, 2004) and cerebral palsy with periventricular leukomalacia (Hoon *et al.*, 2002). The exemplary applications of fiber tractography in clinical research are displayed in Fig. 23.

## XI. Conclusion

In this chapter, I introduced the basics, acquisition, processing, and applications of DTI. This method has provided a unique *in vivo* tool for the exploration of white matter, which lays the groundwork for the understanding of anatomical connectivity in the human brain. DTI has also been regarded as an important tool in the functional neuroimaging area using PET and functional MRI, and thus a growing amount of research has been conducted based on the combination of both imaging modalities. Although we cannot disregard current limitations of DTI, a number of recent techniques have proved its validity and usefulness in clinical applications. The advances in acquisition and postprocessing of DTI will certainly lead to a better understanding of white-matter pathology and contribute to more effective clinical application.

## References

- Alexander, A. L., Tsuruda, J. S., and Parker, D. L. (1997). Elimination of eddy current artifacts in diffusion-weighted echo-planar images: The use of bipolar gradients. *Magn. Reson. Med.* **38**, 1016–1021.
- Basser, P. J., Mattiello, J., and Le Bihan, D. (1994). MR diffusion tensor spectroscopy and imaging. *Biophys. J.* **66**, 259–267.

- Basser, P. J., Pajevic, S., Pierpaoli, C., Duda, J., and Aldroubi, A. (2000). *In vivo* fiber tractography using DT-MRI data. *Magn. Reson. Med.* **44**, 625–632.
- Basser, P. J., and Pierpaoli, C. (1996). Microstructural and physiological features of tissues elucidated by quantitative-diffusion-tensor MRI. *J. Magn. Reson. B* **111**, 209–219.
- Batchelor, P. G., Hill, D. L. G., Atkinson, D., Calamante, F., and Connelly, A. (2002). Fiber tracking by solving the diffusion-convection equation. *Proc. International Soc. Magn. Reson. Med.*, p. 1135. Honolulu, HI.
- Beaulieu, C. (2002). The basis of anisotropic water diffusion in the nervous system - a technical review. *NMR Biomed.* **15**, 435–455.
- Beaulieu, C., and Allen, P. S. (1994). Determinants of anisotropic water diffusion in nerves. *Magn. Reson. Med.* **31**, 394–400.
- Behrens, T. E., Johansen-Berg, H., Woolrich, M. W., Smith, S. M., Wheeler-Kingshott, C. A., Boulby, P. A., Barker, G. J., Sillery, E. L., Sheehan, K., Ciccarelli, O., Thompson, A. J., Brady, J. M., and Matthews, P. M. (2003). Non-invasive mapping of connections between human thalamus and cortex using diffusion imaging. *Nat. Neurosci.* **6**, 750–757.
- Clark, C. A., Barrick, T. R., Murphy, M. M., and Bell, B. A. (2003). White matter fiber tracking in patients with space-occupying lesions of the brain: A new technique for neurosurgical planning? *Neuroimage* **20**, 1601–1608.
- Conturo, T. E., Lori, N. F., Cull, T. S., Akbudak, E., Snyder, A. Z., Shimony, J. S., McIntyre, R. C., Burton, H., and Rachel, M. E. (1999). Tracking neuronal fiber pathways in the living human brain. *Proc. Natl. Acad. Sci. USA* **96**, 10422–10427.
- Dong, Q., Welsh, R. C., Chenevert, T. L., Carlos, R. C., Maly-Sundgren, P., Gomez-Hassan, D. M., and Mukherji, S. K. (2004). Clinical applications of diffusion tensor imaging. *J. Magn. Reson. Imaging* **19**, 6–18.
- Frank, L. R. (2002). Characterization of anisotropy in high angular resolution diffusion-weighted MRI. *Magn. Reson. Med.* **47**, 1083–1099.
- Gembris, D., Schumacher, H., and Suter, D. (2001). Solving the diffusion equation for fiber tracking in the living human brain. Proceedings of the International Society for Magnetic Resonance in Medicine (ISMRM), Glasgow, Scotland, 1529.
- Hagmann, P., Thiran, J. P., Jonasson, L., Vanderghenst, P., Clarke, S., Maeder, P., and Meuli, R. (2003). DTI mapping of human brain connectivity: Statistical fibre tracking and virtual dissection. *Neuroimage* **19**, 545–554.
- Hoon, A. H., Jr., Lawrie, W. T., Jr., Melhem, E. R., Reinhardt, E. M., Van Zijl, P. C., Solaiyappan, M., Jiang, H., Johnston, M. V., and Mori, S. (2002). Diffusion tensor imaging of periventricular leukomalacia shows affected sensory cortex white matter pathways. *Neurology* **59**, 752–756.
- Huppi, P. S., Maier, S. E., Peled, S., Zientara, G. P., Barnes, P. D., Jolesz, F. A., and Volpe, J. J. (1998). Microstructural development of human newborn cerebral white matter assessed *in vivo* by diffusion tensor magnetic resonance imaging. *Pediatr. Res.* **44**, 584–590.
- Jellison, B. J., Field, A. S., Medow, J., Lazar, M., Salamat, M. S., and Alexander, A. L. (2004). Diffusion tensor imaging of cerebral white matter: A pictorial review of physics, fiber tract anatomy, and tumor imaging patterns. *AJNR Am. J. Neuroradiol.* **25**, 356–369.
- Jones, D. K. (2004). The effect of gradient sampling schemes on measures derived from diffusion tensor MRI: A Monte Carlo study. *Magn. Reson. Med.* **51**, 807–815.
- Jones, D. K., Simmons, A., Williams, S. C., and Horsfield, M. A. (1999). Non-invasive assessment of axonal fiber connectivity in the human brain via diffusion tensor MRI. *Magn. Reson. Med.* **42**, 37–41.
- Koch, M. A., Norris, D. G., and Hund-Georgiadis, M. (2002). An investigation of functional and anatomical connectivity using magnetic resonance imaging. *Neuroimage* **16**, 241–250.
- Kubicki, M., Westin, C. F., Maier, S. E., Mamata, H., Frumin, M., Ersner-Hershfield, H., Kikinis, R., Jolesz, F. A., McCarley, R., and Shenton, M. E. (2002). Diffusion tensor imaging and its application to neuropsychiatric disorders. *Harv. Rev. Psychiatry* **10**, 324–336.

- Kubicki, M., Westin, C. F., Nestor, P. G., Wible, C. G., Frumin, M., Maier, S. E., Kikinis, R., Jolesz, F. A., McCarley, R. W., and Shenton, M. E. (2003). Cingulate fasciculus integrity disruption in schizophrenia: A magnetic resonance diffusion tensor imaging study. *Biol. Psychiatry* **54**, 1171–1180.
- Le Bihan, D., Breton, E., Lallemand, D., Grenier, P., Cabanis, E., and Laval-Jeantet, M. (1986). MR imaging of intravoxel incoherent motions: Application to diffusion and perfusion in neurologic disorders. *Radiology* **161**, 401–407.
- Lee, S. K., Mori, S., Kim, D. J., Kim, S. Y., Chu, M., Heo, K., Lee, B. I., and Kim, D. I. (2003). Diffusion tensor MRI and fiber tractography of cerebellar atrophy in phenytoin users. *Epilepsia* **44**, 1536–1540.
- Lee, S. K., Mori, S., Kim, D. J., Kim, S. Y., and Kim, D. I. (2004). Diffusion tensor MR imaging visualizes the altered hemispheric fiber connection in callosal dysgenesis. *AJNR Am. J. Neuroradiol.* **25**, 25–28.
- Maier, S. E., Gudbjartsson, H., Patz, S., Hsu, L., Lovblad, K. O., Edelman, R. R., Warach, S., and Jolesz, F. A. (1998). Line scan diffusion imaging: Characterization in healthy subjects and stroke patients. *AJR Am. J. Roentgenol.* **171**, 85–93.
- Melhem, E. R., Mori, S., Mukundan, G., Kraut, M. A., Pomper, M. G., and van Zijl, P. C. (2002). Diffusion tensor MR imaging of the brain and white matter tractography. *AJR Am. J. Roentgenol.* **178**, 3–16.
- Mori, S., Crain, B. J., Chacko, V. P., and van Zijl, P. C. (1999). Three-dimensional tracking of axonal projections in the brain by magnetic resonance imaging. *Ann. Neurol.* **45**, 265–269.
- Mori, S., Frederiksen, K., van Zijl, P. C., Stieltjes, B., Kraut, M. A., Solaiyappan, M., and Pomper, M. G. (2002). Brain white matter anatomy of tumor patients evaluated with diffusion tensor imaging. *Ann. Neurol.* **51**, 377–380.
- Neil, J., Miller, J., Mukherjee, P., and Huppi, P. S. (2002). Diffusion tensor imaging of normal and injured developing human brain - a technical review. *NMR Biomed.* **15**, 543–552.
- Norris, D. G. (2001). Implications of bulk motion for diffusion-weighted imaging experiments: Effects, mechanisms, and solutions. *J. Magn. Reson. Imaging* **13**, 486–495.
- Papadakis, N. G., Martin, K. M., Pickard, J. D., Hall, L. D., Carpenter, T. A., and Huang, C. L. (2000). Gradient preemphasis calibration in diffusion-weighted echo-planar imaging. *Magn. Reson. Med.* **44**, 616–624.
- Park, H. J., Kubicki, M., Shenton, M. E., Guimond, A., McCarley, R. W., Maier, S. E., Kikinis, R., Jolesz, F. A., and Westin, C. F. (2003). Spatial normalization of diffusion tensor MRI using multiple channels. *Neuroimage* **20**, 1995–2009.
- Park, H. J., Kubicki, M., Westin, C. F., Talos, I. F., Brun, A., Peiper, S., Kikinis, R., Jolesz, F. A., McCarley, R. W., and Shenton, M. E. (2004). Method for combining information from white matter fiber tracking and gray matter parcellation. *AJNR Am. J. Neuroradiol.* **25**, 1318–1324.
- Parker, G. J., Schnabel, J. A., Symms, M. R., Werring, D. J., and Barker, G. J. (2000). Nonlinear smoothing for reduction of systematic and random errors in diffusion tensor imaging. *J. Magn. Reson. Imaging* **11**, 702–710.
- Parker, G. J., Wheeler-Kingshott, C. A., and Barker, G. J. (2002). Estimating distributed anatomical connectivity using fast marching methods and diffusion tensor imaging. *IEEE Trans. Med. Imaging* **21**, 505–512.
- Peled, S., Gudbjartsson, H., Westin, C. F., Kikinis, R., and Jolesz, F. A. (1998). Magnetic resonance imaging shows orientation and asymmetry of white matter fiber tracts. *Brain Res.* **780**, 27–33.
- Pierpaoli, C., Barnett, A., Pajevic, S., Chen, R., Penix, L. R., Virta, A., and Basser, P. (2001). Water diffusion changes in Wallerian degeneration and their dependence on white matter architecture. *Neuroimage* **13**, 1174–1185.
- Pierpaoli, C., and Basser, P. J. (1996). Toward a quantitative assessment of diffusion anisotropy. *Magn. Reson. Med.* **36**, 893–906.
- Poupon, C., Clark, C. A., Frouin, V., Regis, J., Bloch, I., Le Bihan, D., and Mangin, J. (2000). Regularization of diffusion-based direction maps for the tracking of brain white matter fascicles. *Neuroimage* **12**, 184–195.

- Poupon, C., Mangin, J., Clark, C. A., Frouin, V., Regis, J., Le Bihan, D., and Bloch, I. (2001). Towards inference of human brain connectivity from MR diffusion tensor data. *Med. Image Anal.* **5**, 1–15.
- Press, W. H., Teukolsky, S. A., Vetterling, W. T., and Flannery, B. P. (1992). Numerical recipes in C. Cambridge, Cambridge University Press.
- Stejskal, E. O., and Tanner, J. E. (1965). Spin diffusion measurements: Spin echoes in the presence of a time-dependent field gradient. *J. Chem. Phys.* **42**, 288–292.
- Sullivan, E. V., and Pfefferbaum, A. (2003). Diffusion tensor imaging in normal aging and neuropsychiatric disorders. *Eur. J. Radiol.* **45**, 244–255.
- Sundgren, P. C., Dong, Q., Gomez-Hassan, D., Mukherji, S. K., Maly, P., and Welsh, R. (2004). Diffusion tensor imaging of the brain: Review of clinical applications. *Neuroradiology* **46**, 339–350.
- Taylor, W. D., Hsu, E., Krishnan, K. R., and Mac Fall, J. R. (2004). Diffusion tensor imaging: Background, potential, and utility in psychiatric research. *Biol. Psychiatry* **55**, 201–207.
- Tench, C. R., Morgan, P. S., Wilson, M., and Blumhardt, L. D. (2002). White matter mapping using diffusion tensor MRI. *Magn. Reson. Med.* **47**, 967–972.
- Tuch, D. S. (2004). Q-ball imaging. *Magn. Reson. Med.* **52**, 1358–1372.
- Tuch, D. S., Reese, T. G., Wiegell, M. R., Makris, N., Belliveau, J. W., and Wedeen, V. J. (2002). High angular resolution diffusion imaging reveals intravoxel white matter fiber heterogeneity. *Magn. Reson. Med.* **48**, 577–582.
- Tuch, D. S., Reese, T. G., Wiegell, M. R., and Wedeen, V. J. (2003). Diffusion MRI of complex neural architecture. *Neuron* **40**, 885–895.
- Westin, C.-F., Maier, S. E., Mamata, H., Nabavi, A., Jolesz, F. A., and Kikinis, R. (2002). Processing and Visualization for Diffusion Tensor MRI. *Medical Image Analysis* **6**, 93–108.
- Wiegell, M. R., Larsson, H. B., and Wedeen, V. J. (2000). Fiber crossing in human brain depicted with diffusion tensor MR imaging. *Radiology* **217**, 897–903.
- Wimberger, D. M., Roberts, T. P., Barkovich, A. J., Prayer, L. M., Moseley, M. E., and Kucharczyk, J. (1995). Identification of “premyelination” by diffusion-weighted MRI. *J. Comput. Assist. Tomogr.* **19**, 28–33.